Published in final edited form as:

Nat Neurosci. 2024 August ; 27(8): 1489–1504. doi:10.1038/s41593-024-01664-w.

Regulation of cell distancing in peri-plaque glial nets by Plexin-B1 affects glial activation and amyloid compaction in Alzheimer's disease

Yong Huang[1,2,3,14], **Minghui Wang**[2,3,14], **Haofei Ni**[1,4], **Jinglong Zhang**[2,3], **Aiqun Li**[2,3], **Bin Hu**[2,3], **Chrystian Junqueira Alves**[1], **Shalaka Wahane**[1], **Mitzy Rios de Anda**[5], **Lap Ho**[2,3], **Yuhuan Li**[1,6], **Sangjo Kang**[1], **Ryan Neff**[2,3], **Ana Kostic**[5], **Joseph D. Buxbaum**[5], **John F. Crary**[1,7,8,9,10], **Kristen J. Brennand**[11], **Bin Zhang**[2,3,12,*], **Hongyan Zou**[1,13,*], **Roland H. Friedel**[1,13,*]

[1]Nash Family Department of Neuroscience, Friedman Brain Institute, Icahn School of Medicine at Mount Sinai, NY, USA.

[2]Department of Genetics and Genomic Sciences, Icahn Institute of Genomics and Multiscale Biology, Icahn School of Medicine at Mount Sinai, NY, USA.

[3]Mount Sinai Center for Transformative Disease Modeling, Icahn School of Medicine at Mount Sinai, NY, USA.

[4]School of Medicine, Tongji University, Shanghai, China.

[5]Seaver Autism Center, Department of Psychiatry, Icahn School of Medicine at Mount Sinai, NY, USA.

[6]Department of Orthopedics, the Second Affiliated Hospital of Xi'an Jiaotong University, Shaanxi, China.

[7]Department of Pathology, Icahn School of Medicine at Mount Sinai, NY, USA.

[8]Department of Artificial Intelligence and Human Health, Icahn School of Medicine at Mount Sinai, NY, USA.

[9]Mount Sinai Neuropathology Brain Bank & Research Core, Icahn School of Medicine at Mount Sinai, NY, USA.

[10]Ronald M. Loeb Center for Alzheimer's Disease, Icahn School of Medicine at Mount Sinai, NY, USA.

[11]Departments of Psychiatry and Genetics, Wu Tsai Institute, Yale University School of Medicine, New Haven, CT, USA.

---

[*]Corresponding authors: Bin Zhang, bin.zhang@mssm.edu, Hongyan Zou, hongyan.zou@mssm.edu, Roland H. Friedel, roland.friedel@mssm.edu.

Authors Contributions

Y.H., H.N., J.Z., A.L., B.H., C.A., S.W., M.R.A., L.H., Y.L. and S.K. conducted experiments and collected data. M.W. and R.N. performed the bioinformatics analyses. R.H.F., H.Z., B.Z. and Y.H. designed the study. J.D.B., A.K., J.F.C and K.J.B. provided expertise in specific assays. All authors participated in data analyses and manuscript preparation.

[14]These authors contributed equally: Yong Huang and Minghui Wang.

Competing Interests

The authors declare no competing interests.

[12]Department of Pharmacological Sciences, Icahn School of Medicine at Mount Sinai, NY, USA.

[13]Department of Neurosurgery, Icahn School of Medicine at Mount Sinai, NY, USA.

Abstract

Communication between glial cells has a profound impact on the pathophysiology of Alzheimer's disease (AD), but signaling mechanisms remain unclear. Here, we reveal that reactive astrocytes play a role in controlling cell distancing in peri-plaque glial nets, which restricts microglial access to Aβ, a prerequisite to detect and engulf amyloid deposits. This process is governed by axon guidance receptor Plexin-B1, a network hub gene that we have identified in late-onset AD, whose expression levels correlate with plaque burden and disease severity in AD patients. We show that Plexin-B1 is predominantly upregulated in plaque-associated astrocytes in a corona-like pattern. Plexin-B1 deletion in *APP/PS1* mice, an amyloidogenic model of AD, leads to reduced spacing and number of reactive astrocytes and microglia in peri-plaque glial nets, along with a higher coverage of amyloid plaques by glial processes, transcriptional changes, and signaling alterations between glial cells. Furthermore, the smaller footprint of peri-plaque glial nets as a result of Plexin-B1 knockout was associated with lower plaque burden, a shift towards dense-core plaque type, and reduced neuritic dystrophy. Altogether, Plexin-B1 regulates the cellular interaction of peri-plaque astrocytes with microglia to affect AD pathophysiology. Relaxing cell spacing by targeting guidance receptors may present an alternative strategy to attenuate neuroinflammation through enhancing glial access to amyloid and plaque compaction in AD.

Keywords

Alzheimer's disease; Glial net; glial communication; Plexin-B1; cell distancing; reactive astrocyte; disease-associated microglia; amyloid plaque

INTRODUCTION

Alzheimer's disease (AD) remains a major medical challenge with no effective treatment[1]. Cognitive decline and memory loss from neurodegeneration are linked to deposition of extracellular amyloid β (Aβ) and intracellular accumulation of neurofibrillary tangles of phospho-tau[2]. Amyloid plaques represent a pathological hallmark of AD[3], but the governing factors of Aβ deposition, clearance, and plaque compaction are not fully understood.

Glial communication is essential for brain homeostasis and injury responses[4]. Recent advances have unveiled the importance of microglia in engulfing and processing of Aβ[5]. The phagocytic activity of microglia promotes plaque compaction, which limits the exposure of neighboring healthy neurons to Aβ material[6]. Microglial coverage of amyloid plaques also serves as a barrier to reduce exposure of neurotoxic protofibrillar Aβ hotspots to neurites[7]. However, the mechanisms governing microglial access and coverage of Aβ, a prerequisite to detect and engulf amyloid material, are not well-defined.

In AD brains, amyloid plaques are surrounded not only by activated microglia but also by reactive astrocytes that respond to pathological stimuli by upregulating GFAP and extending hypertrophic arborized processes[8]. Reactive astrocytes and microglia closely interact with one another and with Aβ, forming peri-plaque glial nets[9]. While it has been shown that microglia-derived factors (e.g., IL-1α, TNF, and C1q) can induce astrocytes into an inflammatory phenotype[10], less is understood of the signaling pathways controlling the physical contacts of these glial cells with one another and with amyloid plaques. Exploring the governing factors of cellular organization or cytoarchitecture of peri-plaque glial nets may have important ramifications for understanding glial activation and plaque development.

Earlier research on reactive astrocytes in AD has mainly focused on the role of ApoE, GFAP, vimentin, connexins, and STAT3[8], however the gene programs operating in plaque-associated astrocytes remain opaque. Multiscale gene network analysis of large-scale genetic and genomic data in AD patients may provide a new framework to nominate novel molecular players influencing disease mechanisms[11]. Indeed, our recent multi-omics analysis of a Mount Sinai Brain Bank AD patient cohort[12, 13] has identified Plexin-B1 (gene symbol *PLXNB1*) as a hub gene in a subnetwork underlying late-onset AD, but its function in AD pathophysiology remains unclear.

Plexin-B1 is a member of the plexin axon guidance receptor family[14]. In addition to axon pathfinding during neurodevelopment, plexins and their cognate semaphorin ligands also mediate a variety of cell-cell communications in development, adult physiology, and cancer[15–18]. Our recent evolutionary studies revealed a highly conserved domain structure of plexins, particularly the ring-shaped extracellular domain and intracellular Ras-GAP domain[19, 20], in accordance with their roles in mediating cytoskeletal dynamics and cell adhesion via small GTPases. Plexin-B1 knockout (KO) mice are viable and fertile, with no overt neurodevelopmental defects[21, 22]. However Plexin-B1 has importance roles in immune system activation and bone homeostasis in adult physiology[23–25], and its functions in CNS pathology remain largely unexplored.

Echoing our multi-omics gene network analysis, studies from other laboratories have independently implicated Plexin-B1 in AD pathophysiology. For instance, *PLXNB1* was identified as a key node in a gene module highly associated with cognitive decline in AD patients of the ROS-MAP cohort[26]. Proteomics studies revealed a positive correlation of Plexin-B1 protein levels with amyloid plaque load and tau neurofibrillary tangle density in AD patients[27]. Furthermore, single nucleus (sn) RNA-sequencing (-seq) identified *PLXNB1* as one of the top induced genes in astrocytes in early stages of AD[28]. While these omics data link Plexin-B1 to AD, *in vivo* functional data are lacking.

We therefore set out to investigate the functional significance of Plexin-B1 in AD pathology. RNAscope in situ hybridization and immunohistochemistry revealed a predominant upregulation of Plexin-B1 in peri-plaque reactive astrocytes. Genetic deletion of Plexin-B1 in an amyloidogenic AD mouse model resulted in a drastic alteration of the cytoarchitecture of glial nets, with reduced spacing and number of reactive astrocytic and microglia, but higher glial coverage of amyloid plaques. These changes were associated with lower plaque burden, a shift towards dense-core type plaques, and less neuritic dystrophy. Concordantly, Plexin-B1 mutant AD animals showed improved memory performance. Single cell RNA sequencing analysis revealed an impact of Plexin-B1 deletion on activation profiles and signaling communication of astrocytes and microglia. Cell culture assays further established a key role of Plexin-B1 in governing cell spacing of astrocytes, cytokine profiles, and interactions with microglia. Together, our results unveil a role of Plexin-B1 in promoting cell distancing in peri-plaque glial nets, which limits glial coverage of amyloid aggregates, leading to more diffuse plaques and exacerbated neuroinflammation and neurotoxicity.

RESULTS

Plexin-B1 is a hub gene in a subnetwork underlying late-onset AD

To uncover new molecular players underlying AD pathophysiology, we have previously conducted multiscale gene network analyses of transcriptomic and genomic data of AD patients from Mount Sinai Brain Bank (MSBB)[12, 13]. This identified Plexin-B1 (gene symbol *PLXNB1*), an axon guidance receptor, as a hub in a coregulated gene subnetwork underlying late-onset AD (Fig. 1A). The *PLXNB1*-centered gene network was significantly enriched for astrocyte-specific genes (3.6-fold enrichment) and AD upregulated genes (2.9-fold enrichment) (Fig. 1B), supporting a link of Plexin-B1 and astrocyte reactivity in AD. The *PLXNB1* network also showed high enrichment for the gene ontology term “Regulation of small GTPase mediated signal transduction” (6.5-fold enrichment), in accordance with neurodevelopmental plexin signaling through Ras/Rap small GTPases to control cytoskeletal dynamics and cell adhesion[18, 29].

Further analysis of the transcriptomic data of the MSBB AD patient cohort revealed a positive correlation of *PLXNB1* expression levels with amyloid plaque density in superior temporal gyrus and parahippocampal gyrus, two commonly affected areas in AD patients (Fig. 1C).

Our previous transcriptomic analysis of late-onset human AD patients had revealed five AD molecular subtypes – typical (C1, C2), intermediate (B1, B2), and atypical (A) – characterized by combinations of dysregulated pathways[30]. We found that *PLXNB1* was particularly upregulated in C1 and C2, two AD subtypes with enrichment of Aβ-associated gene changes (Fig. 1D, E). Altogether, these multiscale -omics analyses implicate Plexin-B1 in mediating astrocyte reactivity in response to Aβ pathology.

Plexin-B1 is upregulated in peri-plaque astrocytes

As the *PLXNB1* AD gene network was enriched for astrocyte genes, we next examined whether Plexin-B1 is specifically expressed in astrocytes. First, a survey of gene expression databases (brainrnaseq.org)[31, 32] revealed a predominant expression of Plexin-B1 in astrocytes as compared to other cell types in both mouse and human CNS (Fig. 2A). We next analyzed recent snRNA-seq datasets of AD patients from two independent studies[28, 33], both showing a specific upregulation of *PLXNB1* in astrocytes but not other cell types in human AD brains (Fig. 2B).

To further confirm specific expression of Plexin-B1 in astrocytes and to interrogate the spatial relation to amyloid plaques, we performed RNAscope mRNA in situ hybridization (ISH) combined with immunofluorescence (IF) on brain sections of 6 months old *APP/PS1* transgenic mice, an amyloidogenic mouse model of AD[34]. We detected a high density of *Plxnb1* mRNA puncta in peri-plaque GFAP$^+$ reactive astrocytes (Fig. 2C; Fig. S1A). Interestingly, *Plxnb1* mRNA puncta were detected not only in cell somas, but also in hypertrophic processes of reactive astrocytes, signifying local translation, a scenario described for *Gfap* and other key astrocyte genes[35, 36]. In contrast, activated microglia surrounding amyloid plaques contained abundant *Aif1* mRNA puncta (encoding Iba1), but scant *Plxnb1* mRNA puncta (Fig. 2C; Fig. S1A). Hence, *Plxnb1* is preferentially expressed in peri-plaque reactive astrocytes in a mouse model of AD.

Currently available antibodies against Plexin-B1 are not specific for IF on mouse brain sections (we had previously tested four antibodies on KO tissues[37]). We thus took advantage of our *Plxnb1* knockout (PB1-KO) allele, which harbors a lacZ reporter cassette inserted behind promoter and initial exons of *Plxnb1*[38], to assess Plexin-B1 expression. The PB1-KO allele was bred into the amyloidogenic *APP/PS1* mouse line[34] (Fig. S1B). LacZ/X-Gal staining of brain sections from 6 months old *APP/PS1 Plxnb1*$^{+/-}$ mice revealed distinct X-gal signals near amyloid plaques (stained by Congo red; Fig. S1C), signifying an upregulation of Plexin-B1 in peri-plaque areas.

In line with the mouse Plexin-B1 expression data, immunohistochemistry (IHC) analysis of human AD patient samples revealed high Plexin-B1 immunosignals in corona-like patterns around amyloid plaques, consistent with Plexin-B1 upregulation in reactive glial nets (Fig. 2D, E). Baseline Plexin-B1 protein levels in unaffected brain areas were low (Fig. 2D). We extended the IHC analysis to brain specimens from a cohort of 11 AD patients, spanning the spectrum of disease severity, including 3 individuals with no clinical AD symptoms. These patient brain specimens had previously been assessed for clinical "ABC" neuropathology scores: Amyloid plaque score, Braak score for neurofibrillary tangles (NFT), and CERAD score (Consortium to Establish a Registry for AD) for neuritic plaques density[39, 40]. We assigned peri-plaque Plexin-B1 expression level scores (scale 0 to 3), which showed a positive correlation with the "ABC" neuropathology scores (Fig. 2F). Attempts of RNAscope ISH or IF staining for Plexin-B1 on human brain specimens yielded high background signals, likely due to preservation challenges for postmortem tissues. Altogether, transcriptomic and histological data converge on Plexin-B1 induction in peri-plaque reactive astrocytes, which correlates with amyloid plaque burden and disease severity in AD patients.

Plexin-B1 governs cell spacing in peri-plaque glial nets and Aβ plaque coverage

To understand the functional significance of Plexin-B1 upregulation for AD pathophysiology, we next compared the cytoarchitecture of peri-plaque glial nets in *APP/PS1* mice with and without *Plxnb1* deletion. To ensure phenotypic consistency of amyloid deposition[8], all mouse cohorts were bred onto C57BL/6J genetic background.

IF staining for GFAP revealed a striking phenotype of Plexin-B1 deletion for astrocyte reactivity in response to amyloid plaques, with a much smaller footprint of peri-plaque glial nets (Fig. 3A). Specifically, in the cortex of 6 months old *APP/PS1* control mice, amyloid plaques were surrounded by numerous reactive astrocytes extending GFAP^{high} hypertrophic processes, collectively forming a glial net with circular structures extending about two cell layers deep from the plaque. By contrast, in matching cortical areas of *APP/PS1* PB1-KO mice of the same age and same C57BL/6J genetic background, we observed a much smaller footprint of peri-plaque glial nets, with reduced number of reactive astrocytes (over 50%), extending only about one-cell layer deep (Fig. 3A–C; Fig. S2).

In addition, spacing or cell-cell distancing of plaque-associated astrocytes appeared reduced in *APP/PS1* PB1-KO mice, with GFAP$^+$ cells crowding in smaller glial nets (Fig. 3B, C). Notably, astrocytic processes displayed polarization towards amyloid plaques in PB1-KO, with increased contact with amyloid material and higher plaque coverage (Fig. 3B, C). These phenotypes illustrate a central role of Plexin-B1 in controlling cell-cell distancing of astrocytes, resulting in wider spaced and looser peri-plaque glial nets; removing Plexin-B1 led to smaller but more compact glial nets with higher density and increased plaque coverage by astrocytic processes.

Since peri-plaque glial nets consist of both reactive astrocytes and activated microglia[9], we next wondered whether changes in spacing and number of peri-plaque reactive astrocyte from Plexin-B1 deletion might also affect microglia recruitment and organization. IF staining for IBA1, a myeloid-specific marker that is upregulated in activated microglia, revealed reduced number of peri-plaque microglia (IBA1^{high}) in *APP/PS1* PB1-KO mice (Fig. 3B, D). As with reactive astrocytes, the spacing of plaque-associated microglia was also reduced with PB1-KO, resulting in increased microglial density in glial nets and higher microglial coverage of amyloid plaque material (Fig. 3B, D). Hence, Plexin-B1 upregulation in astrocytes affected also microglia in AD glial nets in regard to mobilization, cell distancing, and glial access to Aβ deposits.

The ablation of Plexin-B1 did not overtly affect the baseline homeostatic state of astrocytes or microglia. IF for astrocyte markers GFAP, S100, and Sox9, or microglia marker IBA1 showed similar staining patterns in both cortex and hippocampus of PB1-KO and wild-type (WT) controls (Fig. S3A–C). In unaffected cortical areas of *APP/PS1* mice without amyloid plaques, Plexin-B1 ablation also did not affect the density, tiling patterns, or morphology of GFAP$^+$ astrocytes or IBA1$^+$ microglia (Fig. S3D). Together, these data illustrate that Plexin-B1 induction in peri-plaque areas governs glial cell mobilization and spacing, as well as glial access and coverage of amyloid, thereby impacting cytoarchitecture and footprint of glial nets in AD (Fig. 3E).

Plexin-B1 deletion alters transcriptomic activation profile of reactive astrocytes in AD

To gain a wider perspective on the impact of Plexin-B1 ablation on gene expression in AD-affected brains at early onset, we first performed bulk RNA sequencing (RNA-seq) on the prefrontal cortex of *APP/PS1* mice with or without PB1-KO at 3–4 month of age, an early timeframe of active Aβ deposition without yet full development of amyloid plaques (Fig. S4A). This identified 2,723 differentially expressed genes (DEGs) in *APP/PS1* PB1-KO vs. *APP/PS1* ($P<0.05$) in the prefrontal cortex (Fig. S4B). Pathway analyses demonstrated that upregulated DEGs in PB1-KO were enriched for GO terms related to nervous system development (e.g., cerebral cortex neuron differentiation, sympathetic nervous system development, ganglion development) and synaptic function (e.g., cytoskeleton of presynaptic active zone, transmembrane phosphatase activity) (Fig. S4C). The downregulated DEGs in PB1-KO concerned tissue inflammation and tissue damage (e.g., TNF-activated receptor activity, CD95 death-induced signaling complex, phagolysosome, collagen fibril organization), detection of mechanical stimuli, and protein deacetylase activity (Fig. S4C). Hence, tissue-level transcriptomics illustrate an overall protective effect of Plexin-B1 deletion, with improved neuronal/synaptic function and attenuated neuroinflammation/cell death.

To dissect the cell type-specific roles of Plexin-B1 in AD brains, we next performed single cell (sc) RNA-seq on the prefrontal cortex of *APP/PS1* mice with or without PB1-KO at 6 months of age (Fig. S5A, B). After applying quality control filters, we obtained data from a total of 27,286 cells from four genotypes (WT, PB1-KO, *APP/PS1*, *APP/PS1* PB1-KO) (Fig. 4A; S5C, D). Among the 10 distinct cell type clusters defined by marker gene expression, microglia formed the largest cluster (43%), followed by endothelial cells (22.6%), astrocytes (16.6%), and other cell types with smaller shares, i.e., fibroblasts/smooth muscle cells, macrophages, oligodendrocytes, neurons, pericytes, and ependymal cells (Fig. S5E). Due to technical factors related to single cell dissociation[41], neurons were underrepresented in this analysis.

We first confirmed in our scRNA-seq data that *Plxnb1* was predominantly expressed in the astrocyte cluster, and that expression was efficiently ablated in PB1-KO condition (Fig. 4B, C). We next focused on astrocytes, which could be further partitioned into 9 transcriptionally distinct subclusters (sc-0 to −8) (Fig. 4D). Sc-8 astrocytes showed the strongest association with reactive astrocytes, expressing high levels of *Gfap* and *Vim* (vimentin), both intermediate filament genes highly upregulated in reactive astrocytes, while *Aqp4* (aquaporin-4) was ubiquitously expressed in all subclusters (Fig. 4E). Notably, *Plxnb1* mRNA was also upregulated in sc-8 astrocytes in *APP/PS1* as compared to WT (Fig. 4F), concordant with the above RNAscope, IHC, and other expression data demonstrating a predominant Plexin-B1 induction in peri-plaque reactive astrocytes.

Moreover, sc-8 astrocytes displayed an enrichment for gene signatures of Disease-associated astrocytes (DAA) identified in an AD mouse model[42], reactive astrocytes linked to inflammatory state[10], as well as EAE astrocytes[43] (Fig. 4G). The relatively small size of the DAA-like sc-8 astrocyte cluster is consistent with the much smaller population of peri-plaque astrocytes as compared to astrocyte populations in plaque-free areas in prefrontal cortex of 6 months old *APP/PS1* mice (Fig. 3A).

We next examined the specific impact of Plexin-B1 KO on gene expression in sc-8 astrocytes of *APP/PS1* condition, which identified 514 upregulated and 699 downregulated DEGs (fold change>1.25) (Fig. 4H; Table S1). Pathway analysis revealed that Plexin-B1 ablation resulted in gene upregulation concerning astrocyte projection and myeloid cell migration/activation (in accordance with the glial net phenotypes described above) (Fig. 4I). Plexin-B1 KO also led to upregulation of genes affecting function or activation state of reactive astrocytes, including energy balance (e.g., Response to Leptin, Acetyl-CoA C-acyltransferase), aminophospholipid transport, and flippase activity (Fig. 4I). The downregulated genes in sc-8 astrocytes with Plexin-B1 KO featured protein synthesis, ECM interaction, endocytosis, and Wnt signaling (Fig. 4I). Collectively, transcriptomics on single cell level provided molecular underpinnings of the effect of Plexin-B1 ablation on functional state of reactive astrocytes in AD, featuring not only astrocyte projection and energy balance, but also immune cell recruitment and ECM reorganization.

Plexin-B1 deficiency also affects transcriptional state of disease-associated microglia in AD

We next analyzed the transcriptomic state of microglia in our scRNA-seq data. The microglia could be partitioned into 11 subclusters (Fig. 5A). Sc-9 microglia showed a close association with disease-associated microglia (DAM) described in an AD model[44], evidenced by induction of multiple DAM signature genes (*Lpl, Cst7, Axl, Itgax, Spp1, Cd9, Ccl6,* and *Csf1)* (Fig. 5B). Moreover, marker genes for homeostatic microglia (*Cx3cr1, P2ry12, Tmem119*) were mostly downregulated in sc-9 (Fig. 5C). Hence, sc-9 microglia were representative of DAM in the *APP/PS1* model of AD.

We found that in the *APP/PS1* PB1-KO condition, the proportion of DAM-like sc-9 microglia was reduced when compared to *APP/PS1* control (Fig. 5D). Specifically, while the amyloidogenic *APP/PS1* transgene resulted in a substantial expansion of sc-9 microglia from 1% in WT to 4% in *APP/PS1*, the subcluster sc-9 was reduced to 2% in *APP/PS1* PB1-KO. In the absence of AD pathology, Plexin-B1 KO alone did not affect sc-9 representation. These findings supported attenuated neuroinflammation in AD brains by Plexin-B1 ablation.

Despite reduced representation of sc-9 microglia in *APP/PS1* PB1-KO brain, transcriptomic analyses suggested augmented microglial activation profiles of the DAM-like microglia. Specifically, Plexin-B1 deletion in *APP/PS1* background resulted in 1,075 DEGs in sc-9 microglia (fold change>1.25), with the vast majority being upregulated (1,070) and only 5 downregulated (Fig. 5E). Pathway enrichment analysis showed that the upregulated genes in sc-9 microglia featured microglial cell activation (*Cx3cr1, C1qa*, *Grn, Ifngra, Aif1* (encoding Iba1), *Tnf*), chemoattraction (*Cx3cr1, Ccrl2, Ccr5)*, and host defense response (*Ubb, B2m, Tlr2*) (Fig. 5F). In addition, genes linked to class II MHC protein complex binding (*Cd81, Ywhae, Hsp90ab1*), cell junction disassembly (*C1qb, C1qa, C1qc, Cx3cr1*), purinergic receptor activity (*P2ry12, Gpr34*), and endolysosomal lumen (*Ctss, Ctsb, Lgmn*) were also enriched in sc-9 microglia in *APP/PS1* PB1 KO (Fig. 5F).

Plexin-B1 deficiency alters signaling communication between DAA and DAM

We next leveraged our scRNA-seq data to probe for the impact of Plexin-B1 KO on signaling communication between glial cells in AD. We focused on top ligand-receptor signaling pairs between DAA-like astrocytes (sc-8) and DAM-like microglia (sc-9) in *APP/PS1* condition as identified by Cellphone DB analysis[45]. Results showed that PB1-KO resulted in an overall augmentation of signaling communication from reactive astrocytes to microglia (Fig. S6A), featuring neuroprotection (Prosapin⇾GRP3), chemoattraction (Chemerin⇾CCRL2), cell adhesion (JAM3⇾Integrin aMb2), and lipid metabolism (APOA1⇾ABCA1, APOA1⇾TREM2). Only one ligand-receptor signaling pair was reduced by PB1-KO, involving Plexin ligand Sema4D (i.e., Sema4D⇾CD45).

Conversely, Plexin-B1 KO also affected signaling communications from microglia to astrocytes in *APP/PS1* condition, again with majority showing enhanced signaling (Fig. S6A). This included ligand-receptor pairs concerning cell adhesion

(CADM1⇾CADM1), chemoattraction/repulsion (EFNB1⇾EPHB3, CSF1⇾CSF1R), lipid metabolism (ApoE⇾TREM2, LDL receptor⇾Sortilin1, and phagocytosis (GAS6⇾AXL). Only two pairs were attenuated with PB1-KO, i.e., Sema4D⇾Plexin-B1 (confirming Plexin-B1 deletion, thus serving as positive control) and IGF1 signaling (IGF1⇾IGF1R, IGF1⇾Integrin α6β4) (Fig. S6A).

For validation, we performed IF staining on *APP/PS1* brains, focusing on three receptors (IGF1R, Axl, and Trem2). Results showed a robust expression of these transmembrane receptors around amyloid plaques (Fig. S6B–D). Consistent with the bioinformatic prediction of a reduced IGF1⇾IGF1R signaling in PB1-KO, we found lower levels of IGF1R around amyloid plaques in PB1-KO as compared to control *APP/PS1* (Fig. S6B). The expression levels of Axl and Trem2 appeared comparable in both cohorts, but the spatial patterns appeared more compact in PB1-KO, consistent with reduced footprint of glial cells (Fig. S6C–D).

Plexin-B1-deficient astrocytes display reduced cell spacing and enhanced cell adhesion in primary culture

So far, IHC and scRNA-seq data had demonstrated that Plexin-B1 ablation affected not only cytoarchitecture of glial nets, but also transcriptional responses of DAA-like astrocytes and DAM-like microglia. For further mechanistic insights, we isolated primary astrocytes from PB1-KO mice and littermate controls. Both *Plxnb1*$^{-/-}$ and control astrocytes showed comparable expression of Sox9, a marker of astrocyte lineage[46], and proliferation marker Ki67 (Fig. S7A, B). Cells of both genotypes also displayed nuclear translocation of NF-κB in response to cytokine stimulation (TNFα plus IL-1β) (Fig. S7C).

Strikingly, *Plxnb1*$^{-/-}$ astrocytes displayed a distinct aggregation behavior in 2D culture as compared to control astrocytes, measurable by a higher aggregation rate of Sox9$^+$ nuclei (Fig. 6A). This finding echoed our in vivo results showing reduced cell distancing of peri-plaque astrocytes in *APP/PS1* PB1-KO mice. Phalloidin staining also revealed reduced F-actin and diminished astrocytic processes of *Plxnb1*$^{-/-}$ astrocytes (Fig. 6A), also in line with the in vivo finding of smaller processes of peri-plaque astrocytes in PB1-KO.

The phenotype of increased cell aggregation as result of Plexin-B1 deletion was striking in a 3D hanging drop assay, where *Plxnb1*$^{-/-}$ astrocytes progressively formed much larger aggregates from 24 to 72 hr than WT counterparts (Fig. 6B). Thus, cell culture studies illustrated a central function of Plexin-B1 in governing astrocyte projection and cell-cell adhesion/spacing.

Plexin-B1-deficient astrocytes displayed reduced cytokine expression and altered interaction with microglia

We next tested how cell-cell spacing and cellular contacts mediated by Plexin-B1 might affect astrocyte function. To this end, we first conducted an ELISA array assay to profile cytokine/chemokine expression in *Plxnb1*$^{-/-}$ vs. control astrocytes (Fig. 6C). ELISA showed that Plexin-B1-deficient astrocytes showed reduced expression of 12 proteins, including CSF-1, a major cytokine for myeloid cell stimulation[47], and ICAM-1, which acts as an inflammatory mediator in the CNS that stimulates the production and secretion of interleukins[48] (Fig. 6C). Of interest in the context of AD was also the downregulation of SerpinE1 (plasminogen activator inhibitor), whose inhibition has been proposed as a therapeutic strategy to reduce amyloid load[49]. Also featured in the ELISA assay was the reduction of several factors linked to IGF signaling, including IGFBP-2, IGFBP-3, and IGFBP-5, echoing the above Cellphone DB analysis as well as IF showing reduced IGF signaling in glial communication in *APP/PS1* PB1-KO condition (see Fig. S6A, B). Of note, elevated IGFBP levels have been associated with more severe outcomes in AD patients by inhibiting the neuroprotective effects of IGF proteins[50].

Since altered lipid signaling by PB1-KO had been indicated by Cellphone DB analysis, we also tested in primary astrocytes the impact of Plexin-B1 KO on the secretion of ApoE, a key lipid metabolism gene and a risk factor for AD[1]. We measured secreted ApoE protein by ELISA, revealing a significantly higher ApoE secretion from *Plxnb1*$^{-/-}$ astrocytes than control counterparts at baseline condition (Fig. S7D). Stimulation with Aβ peptides led to increased ApoE secretion from control astrocytes but did not further enhance the already high levels of ApoE secretion of PB1-KO astrocytes (Fig. S7D).

Given the reduced cytokine/chemokine expression and decreased cell-cell spacing of Plexin-B1-deficient astrocytes, we next examined its impact on their interaction with microglia. We co-cultured primary astrocytes (control or *Plxnb1*$^{-/-}$) with primary WT microglia for 2 days and examined their spatial arrangement by co-IF staining for GFAP and IBA1. In control co-cultures, astrocytes extended long and slender processes, while microglia formed distinct clusters (Fig. 6D). In comparison, *Plxnb1*$^{-/-}$ astrocytes seemed to have less influence on the patterning of microglia (Fig. 6D), in line with reduced cytokine/chemokine expression by *Plxnb1*$^{-/-}$ astrocytes. Collectively, these cell culture results supported the model of reduced glial mobilization and attenuated neuroinflammation in PB1-KO condition.

Plexin-B1 affects cellular interaction of human iPSC-derived astrocytes with human microglia

To probe for the applicability of our findings in mouse models for human cells, we employed CRISPR/Cas9 genome editing to delete *PLXNB1* in human induced pluripotent stem cells (hiPSCs) (Fig. S8A). We generated two pairs of isogeneic hiPSC lines (from two control donors) with and without deletion of *PLXNB1*, confirmed by DNA sequencing (Fig. S8A). We then induced differentiation of hiPSCs into astrocytes (iAstro) by viral expression of *NFIB* and *SOX9*[51] (Fig. S8B). IF staining revealed that Plexin-B1 deletion did not seem to affect astrocyte differentiation from hiPSC, shown by comparable expression of astrocyte markers (S100, Sox9, GFAP) and similar morphology (Fig. S8C–E).

We next co-cultured iAstro with human GFP-expressing microglia for 3 days, and IF staining showed that wild-type iAstro influenced the spatial patterning of microglia, leading to distinct aggregation patterns, whereas such patterns were much less apparent in co-cultures with *PLXNB1*-deficient iAstro (Fig. S8F–H).

Plexin-B1 deletion leads to reduced amyloid burden and a shift towards dense-core plaque type

We next examined how the changes of glial net architecture and activation profiles of glial cells in Plexin-B1 KO might impact Aβ plaque development/clearance and associated neurotoxicity. Histological inspection of amyloid plaques revealed a significant reduction of plaque burden in 6 months old *APP/PS1* PB1-KO mice as compared to age-matched *APP/PS1* controls (Fig. 7A; S9A). Moreover, plaques in KO appeared smaller, with average size reduced by almost 50% (Fig. 7A). A plaque size distribution analysis further confirmed that PB1-KO resulted in a shift of amyloid plaques towards smaller sizes (Fig. 7C).

We further surveyed the composition of amyloid plaques by co-staining with anti-Aβ antibody 6E10 (which labels most amyloid plaques) and Thio-S dye (which stains amyloid plaque cores)[7] (Fig. 7B). This co-staining method allowed us to classify plaques by compaction type (Fig. 7D). We found that in the cortex of *APP/PS1* mice, close to 50% plaques were fibrillar type, 35% mixed, and 15% dense-core; by contrast, in *APP/PS1* PB1-KO mice the composition was reversed (15% fibrillar, 35% mixed, and 50% dense-core type) (Fig. 7D). As dense-core plaque formation is an outcome of efficient microglial phagocytosis of amyloid material[52], the shift of plaques towards dense-core in PB1-KO mice thus agrees with our observations of increased microglial coverage of plaques and augmented microglial function in PB1-KO.

Plexin-B1 deletion leads to reduced neurotoxicity and improved memory performance

Amyloid plaques are typically surrounded by a halo of dystrophic neuronal membranes[7]. To gauge neurotoxicity of amyloid plaques, we performed IF staining for LAMP1, an autophagy and endolysosomal marker that is highly enriched in dystrophic neurites[53, 54]. We found a 50% reduction in the number of LAMP1-labeled areas in the cortex of *APP/PS1* PB1-KO vs. *APP/PS1* mice (Fig. 8A; S9B), echoing the overall reduction of plaque burden in PB1-KO. The average size of LAMP1-marked halos around amyloid plaques was also reduced in PB1-KO (Fig. 8A).

We also conducted IF staining for autophagosome protein ATG9A, a marker of dystrophic neurites[55]. This revealed a significant reduction of both the size and number of ATG9A-labeled areas near plaques (Fig. 8A). The reduced neuritic dystrophy observed in *APP/PS1* PB1-KO mice aligned with the model that dense-core plaques correspond to reduced neurotoxicity due to limited dissemination of neurotoxic soluble Aβ oligomers[52].

We next assessed the expression of CD68[56], which labels phagocytic microglia. We detected a comparable ratio of CD68$^+$ areas relative to Aβ-labeled plaque areas in *APP/PS1* PB1-KO and *APP/PS1* mice (Fig. 8B). Hence, the abundance of phagocytic microglia was not expanded in PB1-KO, but they were confined in smaller glial nets, with improved access to amyloid deposits.

Lastly, we conducted Barnes Maze behavioral assays, comparing memory performance of aged cohorts of *APP/PS1* and *APP/PS1* PB1-KO mice. Resulted showed that PB1-KO was associated with improved working memory performance during the acquisition training trials (Fig. S10A), while memory recall performance in probe trials was similar between cohorts (Fig. S10B).

DISCUSSION

Mobilization of astrocytes and microglia in peri-plaque reactive glial nets is critical to clear Aβ, control neuroinflammation, and limit neurotoxicity. A prerequisite to detect and engulf Aβ amyloid material is an adequate coverage of the amyloid plaque by glial processes, which involves morphological transformation of astrocytes and microglia upon contact with Aβ amyloid[52]. Insufficient access to amyloid deposits by glial processes results in poor Aβ clearance, more diffuse fibrillar plaques, and increased neurotoxicity, which may trigger a detrimental cycle of recruitment of more glial cells, heightened inflammation, and a larger footprint of reactive glial nets.

Our study revealed that axon guidance receptor Plexin-B1 is upregulated in astrocytes of peri-plaque glial nets in a corona-like pattern, and it is engaged in glial cell mobilization and cell distancing around amyloid plaques. Intriguingly, we observed that in the absence of Plexin-B1, cell distancing in peri-plaque nets was reduced, while plaque coverage by glial processes was improved. This may initiate a positive cycle of better Aβ clearance, a shift towards dense-core plaques, less neurotoxicity, thus a reduced need for more glial mobilization and thereby an overall smaller footprint of glial nets (Fig. 8C). Compact Aβ plaques have been suggested as a neuroprotective response of the immune system to encapsulate foreign bodies, akin to granulomas[57]. In support of improved efficiency of glial cells to clear Aβ deposits, our scRNA-seq data revealed that Plexin-B1 deletion led to transcriptional changes linked to enhanced activation profiles of disease-associated astrocytes and microglia, as well as augmented ligand-receptor signaling communication, featuring chemoattraction, ECM remodeling, and lipid metabolism.

Our study showed that Plexin-B1 is predominantly expressed in peri-plaque astrocytes, yet its deletion affected the cytoarchitecture of both astrocytes and microglia in AD reactive glial nets. Although we cannot exclude potential effects from low expression of Plexin-B1 in microglia, a more likely explanation for microglial phenotypes in Plexin-B1 KO is a secondary effect from altered chemoattraction/glial cell spacing and an overall attenuated inflammatory milieu in the peri-plaque glial nets. Moreover, in absence of Plexin-B1, relaxed cell distancing may physically permit closer access of microglia to plaques, which in turn elicits morphological and transcriptomic transformation of microglia to a DAM state[44]. In support, our primary cell culture studies illustrated a central function of Plexin-B1 in controlling cell spacing of astrocytes, as well as cytokine expression profiles and microglia clustering.

Plexin signaling is best known for growth cone collapse during neurodevelopment; recent studies from our laboratory and others have further unveiled a role of Plexins in cell collision guidance[58, 59]. This process, termed contact inhibition of locomotion (CIL), has also been reported for Plexin-B1 mediated physical contact between osteoclasts and osteoblasts[58]. The phenotypes in the current study are thus consistent with the working model that Plexin-B1 imposes cell distancing in peri-plaque glial nets by promoting contact avoidance.

The molecular identity and cellular source of the activating signals for Plexin-B1 in AD brains require further studies. Plexin-B1 binds to class 4 semaphorins, a family with six ligands expressed in diverse cell types[17, 60]. A recent study in a mouse model of multiple sclerosis (MS) showed that Sema4D expressed by microglia can activate Plexin-B1 and -B2 expressed in astrocytes[61]. Conceivably, in AD brains, Sema4D expressed by microglia may activate Plexin-B1 on astrocytes to maintain cell distancing. Interestingly, a recent study also reported a semaphorin-independent mechanosensitive function for Plexin-D1, a paralog of Plexin-B1, to detect blood flow shear stress in endothelial cells[62]. This raises an interesting alternative scenario that Plexin-B1 may function to sense mechanical forces originating from distorted interstitial space near amyloid plaques.

In line with the notion that strategies to promote microglial phagocytosis may benefit AD patients, future therapies targeting Plexin-B1 to increase glial plaque coverage and glial cell communication may attenuate AD pathophysiology, regardless of whether the beneficial effect is exclusively from reactive astrocytes or other glial cells. In this context it is noteworthy that while small molecule inhibitors of plexin signaling are currently unavailable, a function-blocking antibody against Sema4D is being tested in a clinical trial for AD[63], and a nanobody blocking Plexin-B1 has recently been developed[64]. Another viable approach to block Plexin-B1 is to employ cyclic peptides acting as allosteric inhibitors[65].

In summary, our data demonstrate a role of reactive astrocytes, through guidance receptor Plexin-B1, in regulating glial mobilization and enforcing cell distancing in peri-plaque glial nets, leading to restricted glial coverage of Aβ deposits, more diffuse amyloid plaques, and increased neural tissue damage. Inhibition of Plexin-B1 may represent an alternative therapeutic approach to reverse this process to benefit AD patients.

METHODS

Construction of *PLXNB1*-centered gene subnetwork

PLXNB1-centered gene subnetwork was extracted from an AD multiscale gene network we previously constructed from the transcriptomic and genomic data of human AD patients and healthy controls in the Mount Sinai Brain Bank (MSBB) cohort[12, 13]. Details about the MSBB cohort data and the methods for building this AD multiscale gene network were described in ref.[12]. Briefly, we built a Bayesian probabilistic causal network from the RNA-seq gene expression data in the parahippocampal gyrus brain region of 215 subjects in the MSBB cohort by using a computational procedure based on the software tool RIMBANet[66, 67]. In the network analysis, we made use of expression quantitative trait loci (eQTLs) computed from the MSBB AD cohort and known transcription factor (TF)-target relationships from the ENCODE project for inferring regulatory relationships between genes. From the full Bayesian network, we extracted the *PLXNB1*-centered gene subnetwork to include only nodes that are up to three steps away from *PLXNB1*.

Analysis of human AD snRNA-seq datasets

For the analysis of snRNA-seq data of human AD patients from Mathys et al., we downloaded the pre-filtered UMI count matrix and associated annotation data (including cell type annotation) from the Synapse data portal (accession # syn18485175) released by the original publication[28]. We further discarded cells with too few (≤ 200) or too many (≥ 6,000) genes detected. The filtered data was analyzed with the Seurat package[68]. Briefly, the UMI data was first normalized by sequencing depth and log-transformed using the LogNormalize method. Taking advantage of cell type annotations provided by the original publication[28], differential expression between AD and control cells were performed for each major brain cell type using the MAST method in Seurat.

For the analysis of Zhou et al. snRNA-seq data, we downloaded the UMI count matrix data from Synapse (accession # syn21125841)[33]. We first performed QC by keeping cells with the following criteria: 200 < number of genes < 2,500, 1,000 < number of UMI counts < 10,000, and percentage of mitochondrial reads < 5%. Only those genes detected in at least two cells were retained. After QC, the UMI data was normalized by sequencing depth and log-transformed using the LogNormalize method implemented in Seurat. The 2,000 most variable gene features were identified, scaled and centered, and subsequently used to calculate principal components (PCs). Top PCs collectively explaining more than 90% of the variance were selected for integrating sequencing libraires using the Harmony package under default parameter settings[69]. The embeddings (dimensional reductions) derived from Harmony were used for calculating UMAP and cell clustering in Seurat. For each cluster, we calculated signatures by comparing the cells in the cluster against the cells of the rest using Wilcox rank sum test. Next, we interrogated the expression patterns of known marker genes to annotate clusters for major brain cell types: excitatory neurons (*SLC17A6*, *SLC17A7*), inhibitory neurons (*GAD1*, *GAD2*), astrocytes (*AQP4*), oligodendrocytes (*MOG*), microglia (*TMEM119*, *TREM2*, and *TYROBP*), oligodendrocyte progenitor cells (*VCAN*), endothelial cells (*FLT1*), and pericytes (*PDGFRB*). Differential expression analyses between AD (*TREM2* common variant only) and control cells were performed for each major brain cell type using the MAST method in Seurat.

Mice

All animal procedures were conducted in accordance with protocols approved by the Institutional Animal Care and Use Committee (IACUC) of Icahn School of Medicine at Mount Sinai. All mouse strains were bred on C57BL/6J genetic background by regular backcrossing with C57BL/6J wild-type mice obtained from the Jackson Laboratory (JAX).

Mouse mutant lines used to breed experimental cohorts:

APP/PS1 transgenic line Tg(APPswe,PSEN1dE9)85Dbo[34], JAX strain MMRRC_034829-JAX;

Plexin-B1 KO line *Plxnb1*$^{\mathrm{tm1Matl}}$ [37], MGI allele MGI:3765917; this KO line carries a lacZ-IRES-PLAP reporter inserted into the *Plxnb1* locus[38].

The *APP/PS1* transgene insertion is located about 4 Mb away from the *Plxnb1* gene locus on chromosome 9, which creates a partial linkage of *Plxnb1* with the *APP/PS1* transgene, and breeding schemes were adjusted in some cases by using cis-heterozygous *APP/PS1*/+ *Plxnb1*$^{+/-}$ breeders.

Histology

All tissue samples were obtained de-identified under approved Institutional Review Board (IRB) protocols under consultation with the Ethics Committee of the Medical Board at the Mount Sinai Hospital. For analysis of post-mortem brain tissues of AD patients by immunohistochemistry (IHC), microtome sections of FFPE (formalin-fixed paraffin-embedded) tissue blocks with associated information about patient age, clinical symptoms, and “ABC” neuropathology score[39, 40] were provided by the Mount Sinai Neuropathology Brain Bank. IHC was performed with an automated Ventana staining device (Roche) with the following primary antibodies: anti-Plexin-B1 (host: rabbit, Sigma HPA040586, 1:50 dilution) anti-Aβ amyloid (host: mouse, clone 4G8, BioLegend 800701, 1:100 dilution). Secondary antibodies were HRP and AP coupled antibodies from the Discovery reagent line for the Ventana staining system (Roche).

For analysis of mouse brain tissues by immunofluorescence (IF), cryopreserved brains were sectioned on a cryostat at 20 μm thickness and collected as floating sections in PBS for storage at 4°C. For IF staining, sections were incubated with blocking buffer (5% normal donkey serum (Jackson ImmunoResearch) and 0.3% Triton X-100 in PBS) for one hour at room temperature prior to overnight incubation at 4°C with primary antibodies in antibody dilution buffer (1% BSA (Fisher Bioreagents) and 0.3% Triton X-100 in PBS).

Primary antibodies for IF of tissue sections and fixed cells in culture dishes:

anti-β-amyloid (host: mouse, clone 6E10, BioLegend 803015, 1:800),

anti-ATG9A (host: rabbit, Abcam ab108338, 1:100),

anti-IBA1 (host: rabbit, Wako Laboratory Chemicals 019–19741, 1:500),

anti-IBA1 (host: goat, Novus Biologics NB100–1028, 1:250),

anti-GFAP (host: rabbit, Dako Z0334, 1:800),

anti-LAMP1 (host: rat, clone 1D4B, DSHB, 1:200),

anti-CD68 (host: rat, clone FA-11, Bio-Rad MCA1957GA, 1: 500),

anti-NF-κB (host: rabbit, Cell Signaling Technology 8242, 1:500),

anti-Ki67 (host: rabbit, Abcam ab16667, 1:250),

anti-GFAP (host: chicken, Aves Labs GFAP, 1:500),

anti-Sox9 (host: rabbit, EMD Millipore ab5535, 1:1,000),

anti-S100 (host: mouse, Sigma S2532, 1:500),

anti-Axl (host: goat, R&D systems AF854, 1:200), anti-Trem2 (host: sheep, R&D systems AF1729, 1:500),

anti-IGF1R (host: goat, R&D systems AF-305, 1:250).

After three washes with PBS, sections were stained for 2 hours with Alexa-488, −594, or −647 conjugated secondary antibodies (Jackson ImmunoResearch: host species donkey, cross-absorbed against IgG of other species). DAPI (Invitrogen) was used for nuclear counterstain. Sections were mounted with Fluoromount-G (Southern Biotech) onto SuperFrost Plus glass slides (VWR).

Antigen retrieval was performed prior to immunostaining for amyloid and tau aggregates. Floating sections were treated with 50% formic acid (Sigma F0507, diluted with distilled water) for 20 minutes and then washed three times with PBS (5 minutes per wash). Subsequently, phospho-Tau or amyloid-beta protein (Aβ) was detected by IF.

Thioflavin S (Sigma T1892) staining of amyloid plaques was performed by staining floating brain sections after IF with 0.005% Thioflavin S solution (in tris-buffered saline, TBS) for 8 minutes. Differentiation of the dye was carried out by two rounds of incubation in 50% ethanol for one minute each. Sections were washed for 5 minutes in TBS and then mounted with Fluoromount-G mounting medium.

RNAscope mRNA in situ hybridization

The mRNAs of mouse genes *Plxnb1* and *Aif1* (encoding Iba1) were co-detected in brain cryosections (12 μm thickness) by RNAscope multiplex ISH (ACD Bio-Techne), using as primary probes Mm-*Plxnb1* (probe ID: 469241) and Mm-*Aif1*-C3 (319141-C3). Hybridization with RNAscope detection reagents and co-immunofluorescence staining with anti-GFAP (Dako Z0334) and anti-β amyloid (clone 6E10, BioLegend 803015) antibodies and donkey secondary antibodies (Jackson ImmunoResearch) were performed according to manufacturer's instructions at the Epigenetics Core Facility of the CUNY Advanced Science Research Center, New York. Nuclei were stained with DAPI. The five fluorescent colors of stained sections were separated by imaging with a confocal Leica Stellaris SP8 microscope with white light laser.

Image analysis

Quantitative analyses of immunofluorescence images for number, area, and signal intensities were performed with ImageJ software (FIJI package). For classification of amyloid plaques into fibrillar, mixed, and dense core types, thioflavin staining patterns were observed and matched to reference examples shown in Fig. 7D.

X-Gal and Congo-Red staining

β-galactosidase reporter expression was identified histochemically by X-Gal assay. X-gal staining solution was prepared by adding X-Gal (dissolved in dimethylformamide) at 1 mg/ml to staining buffer (0.02% Igepal, 0.01% sodium deoxycholate, 5 mM potassium ferricyanide, 5 mM potassium ferrocyanide, and 2 mM MgCl2 diluted in 0.1 M PBS (pH 7.3)). 6-month-old APP mice were perfused with 4% PFA/PBS, brains were post-fixed for 6 hours in and embedded in 4% agarose/PBS for vibratome sectioning and stored at 4°C.

100 µm thick brain sections were collected and were incubated overnight in X-gal staining solution at 37°C. Slides were then dipped sequentially in 70% ethanol for 5 minutes, followed by 100% ethanol for 10 minutes and lastly 70% ethanol for 1 minute before hydrating them in water. Slides were then incubated in a 1% aqueous Congo Red solution (Sigma C6277) for 30–60 minutes at RT followed by rapid differentiation (5–10 dips) in alkaline alcohol solution (1% NaOH, 50% ethanol), and rinsed in running water for 10 minutes.

Primary astrocytes

Primary astrocyte cultures were generated from postnatal day 1–3 pups. After removal of meninges, forebrains were dissected, cut into small pieces, rinsed in HBSS, and centrifuged at 300 g for 3 min. The pelleted tissue pieces were processed using the Miltenyi Neural Tissue Dissociation Kit-T (Miltenyi 130-093-231) following the manufacturer's protocol to obtain a culture of mixed neural cells. Specifically, the tissue pieces were incubated in 2 ml of enzyme mixture 1 for 30 min at 37 °C (200 µl enzyme T in 1.75 ml buffer X) with gentle shaking by hand every 5 min. Then, 30 µl of enzyme mixture 2 (10 µl enzyme A in 20 µl buffer Y) was added to the cell suspensions, which was manually triturated (slowly, 10 times per sample) with a large-opening (1,000 µm diameter) fire-polished pipette. After incubation for 10 min at 37°C, suspensions were triturated with a medium- and then small-opening (750 µm and 500 µm diameter, respectively) fire-polished pipette to produce single-cell suspensions. Suspensions were strained through a 70 µm cell strainer and washed with 10 ml HBSS with Ca^{2+} and Mg^{2+} solution. Cells in suspensions were pelleted at 300 g for 10 min and resuspended and plated in DMEM/Glutamax media with 10% FBS and 1:100 Pen/Strep (Gibco) and cultured to 90% density in 6-well plates.

Astrocytes were further enriched using an anti-ACSA-1 MicroBead Kit (Miltenyi 130-095-826). Briefly, primary astrocytes were prepared in single cell suspension, incubated with anti-ACSA-1 microbeads and separated with MS magnetic columns (Milteny Biotec #130-042-201).

For standard imaging experiments, astrocytes were seeded at a density 4×10^4 cells per well into 24-well plates containing glass coverslips coated with poly-L-ornithine (PLO) (Sigma, 30% solution) for 1 hr at 37°C, rinsed once with PBS, and then laminin coating (Invitrogen, 10 µg/ml) for 1 hr at 37°C. Cells were fixed 48 hours after seeding with 3.7% formaldehyde/PBS for 10 min at room temperature. Staining by immunofluorescence was performed following protocol described above.

Cytokine ELISA

For proteome profiler assay (cytokine array), ACSA-1 microbead enriched astrocytes were collected, and protein was extracted (1×10^7 cells/ml) using Lysis Buffer 17 (R&D Systems 895943) supplemented with 10 µg/ml aprotinin (Tocris 4139), 10 µg/ml leupeptin (Tocris 1167) and 10 µg/ml pepstatin (Tocris 1190). Cell lysates were applied to the cytokine array (Proteome Profiler Mouse XL Cytokine Array, R&D Systems, ARY028) following manufacturer's instructions. Membrane images were captured using an iBright 1500 Imaging System (Thermo Fisher) and analyzed using ImageJ.

Primary microglia

The initial steps of microglia preparation were performed following the protocol described above for primary astrocyte with Miltenyi Neural Tissue Dissociation Kit-T (cat # 130-093-231) to generate mixed neural cells. Cells were seeded onto high-attachment 6-well Primaria plates (Corning 08-772-4J) in DMEM/Glutamax media with 10% FBS and 1:100 Pen/Strep (Gibco) at a density of 1.5 million cells per well. Medium was changed once a week and cells were kept in culture for up to 4 weeks. Typically, 2 week old cultures were used for experiments. To separate microglia from neurons and astrocytes, 1 ml of 0.25% Trypsin-EDTA was added to the 6-well plate and incubated at 37°C for 5 min. Neurons and astrocytes would delaminate first, leaving the highly adherent microglia behind. Supernatant was removed and either used for subsequent experiments or discarded. Another 1 ml 0.25% Trypsin-EDTA was added per well to detach microglia by incubating cells at 37°C for 10 min. This method yielded ~90% pure microglia with minimal neural cell contamination.

For co-culture studies of microglia with astrocytes, 2×10^4 microglia and 2×10^4 astrocytes were seeded into 24-well plates containing glass coverslips coated with poly-L-ornithine (PLO) (Sigma) and laminin (Invitrogen) and processed for imaging as described above.

Cell aggregation assay in hanging drop

For cell aggregation assay, the hanging drop method was used, wherein 2×10^4 dissociated astrocytes were seeded in a 10 μl droplet in DMEM/Glutamax media with 10% FBS and 1:100 Pen/Strep (Gibco) on an inverted lid of a 6-cm tissue culture dish. The lid was returned to the corresponding 6-cm culture dish filled with 5 ml PBS to maintain humidity during incubation. Photos of hanging drops were taken at 24, 48 and 72 hours after seeding with a stereomicroscope. The number of spheres in each drop were quantified using ImageJ. Eight drops for each group at three different time points were quantified, and three independent experiments were performed.

ApoE ELISA assay

For treatment of cells with oligomerized Aβ amyloid (oAβ), β amyloid (1–42) (Bachem 4061966) was dissolved in hexafluoro-isopropanol (MP Biomedicals 0215124505) to obtain 1 mM solution. Solvent was then evaporated from the solution by Speedvac centrifugation. Dried Aβ amyloid was re-suspended in DMSO to obtain 5 mM solution, sonicated in water bath for 10 minutes, diluted in PBS to a concentration of 50 μM, and stored at 4°C for 12 hours before adding to the cells.

For ApoE ELISA, astrocytes were seeded in 24 well plates at a density of 30,000 cells per well. After 24 hours, cells were cultured with serum free DMEM medium with vehicle (0), 2, 5, and 10 μM oAβ. After 24 hours, supernatant was collected and secretion of ApoE protein into the cell culture supernatant was measured with an ApoE ELISA kit (Mybiosource MBS705227).

Human induced pluripotent stem cells and human microglia

Human iPSCs (CP1: 553-S1–1, CP2: 2607-1-4) were originally generated by Dr. Kristen Brennand’s laboratory at the Icahn School of Medicine at Mount Sinai. These hiPSCs are part of the National Institute of Mental Health (NIMH) childhood-onset schizophrenia (COS) cohort (NSB553, NSB2607). Human microglia were purchased from AcceGen Biotech (ABC-TC3704). The microglia were transduced with lenti-gRNA-Library_eGFP, a gift from Jose Silva (Dep. of Oncological Sciences, Icahn School of Medicine at Mount Sinai) to constitutively expresses GFP. All research involving hiPSCs was carried out under the supervision and approval of the Institutional Review Board (IRB) and the Embryonic Stem Cell Research Overview (ESCRO) committees at the Icahn School of Medicine at Mount Sinai. Informed consent was obtained from all skin cell donors as part of a study directed by Judith Rapoport MD at the National Institute of Mental Health (NIMH).

Generation of isogenic pairs of *PLXNB1* knockout hiPSCs

Three gRNAs targeting *PLXNB1* exon 3 were obtained through the Mount Sinai CRISPR Initiative Program. Details on the sgRNA sequences:

Oligo ID	Location	gRNA sequence	PAM
PLXNB1_1	48424318 – 48424340	ATTCGGGTTGTTGGTAGGCT	GGG
PLXNB1_2	48424317 – 48424339	GATTCGGGTTGTTGGTAGGC	TGG
PLXNB1_3	48424313 – 48424335	AGCTGATTCGGGTTGTTGGT	AGG

These gRNAs were individually packaged into lentiviruses using a third-generation packaging system and then transduced into hiPSCs expressing Cas9 constitutively (lentiCRISPR v2, Addgene #52961). Following antibiotic selection, a limited number of single hiPSCs were plated in 10-cm dishes. After one week, single hiPSC clones were selected and expanded. Subsequently, genome samples were prepared and amplified using primers targeting the gene editing region. Successful gene editing was confirmed through Sanger sequencing of PCR products cloned into plasmids using TOPO cloning.

hiPSC-astrocyte induction

Two isogenic pairs of hiPSCs were maintained in Stemflex media (Thermo Fisher A3349401) on Matrigel (Corning #354230) coated plates. On day −2, hiPSCs were seeded at a density of 3×10^5 cells per well in a 12-well plate, with coverslips placed in the plate if immunofluorescence was required. On day −1, hiPSCs were transduced with rtTA, TetO.Sox9.puro (Addgene #117269), and TetO.NfiB.Hygro (Addgene #117271) by spinfection. After 10 hours, the medium was switched to a non-viral one. On day 0, 2.5 μg/ml doxycycline (Dox) was added to induce SOX9 and NFIB expression. On day 1, transduced hiPSC-astrocytes were treated with dual antibiotics (1 μg/ml puromycin and 200 μg/ml Hygromycin B) to select for transduced astrocytes. These cells were expanded in Expansion Medium (DMEM/F-12, HEPES, 1x N2, 10% FBS, and 1x Glutamax) with the addition of 2.5 μg/ml Dox. On day 3, the Expansion Medium was replaced with Astrocyte FGF medium, consisting of Neurobasal, 1x B27, 1x MEM Non-Essential Amino Acids Solution, 1x Glutamax, 1% FBS, 8 ng/ml FGF2, 5 ng/ml CNTF, and 10 ng/ml BMP4, all supplemented with 2.5 μg/ml Dox. On day 8, the FGF2 medium was transitioned to Astrocyte Maturation Medium (DMEM/F12 HEPES and Neurobasal, 1% Sodium Pyruvate, 1x N2, 1x Glutamax, 5 μg/ml N-acetyl-cysteine, 5 ng/ml Heparin-binding EGF-like growth factor, 10 ng/ml CNTF, 10 ng/ml BMP4, and 500 μg/ml dibutyryl cyclic-AMP), with 2.5 μg/ml Dox. On day 11, Dox was completely withdrawn via a full medium change, followed by subsequent half medium changes. hiPSC-astrocytes were harvested approximately between day 21 and 24.

Quantification of astrocyte aggregation rates

The rate of astrocyte aggregation was quantified using ImageJ software. Initially, the ‘Analyze Particles’ function was employed to sequentially label all Sox9$^+$ nuclei. Subsequently, the ‘Graph’ plugin (https://imagej.nih.gov/ij/plugins/graph/index.html) was used to create an adjacency list based on the separation distance between nuclei. After setting a threshold distance of 35 μm for nuclei centroids of astrocytes, labeled particles (i.e., nuclei) that are less than 35μm apart were grouped into subgraphs and counted as a single connected component. Fewer connected components suggest a higher rate of aggregation. The value of 1 - (connected components/ total nuclei) was utilized to represent the astrocyte aggregation rate.

The rate of microglia aggregation was quantified as described above with slight modifications. Microglia nuclei were identified among co-cultured astrocytes based on higher DAPI staining intensity and relatively smaller size. Accordingly, “threshold” and “particle size” parameters were adjusted in ImageJ so that only microglia nuclei were selected for connected component analysis. A distance of 15 μm was set for the “Graph” plugin as the threshold to qualify neighboring nuclei centroids as connected.

Barnes maze behavioral assay

The Barnes maze study was conducted using a mouse elevated Barnes maze apparatus (Stoelting 60170), which is comprised of a gray non-reflective elevated circular platform (91 cm in diameter) with 20 holes that are equally spaced along the edge of the platform. Our testing protocol followed the general protocol as described in ref.[70]. In brief, mice were first subjected to a habituation phase to acclimate animals to the elevated platform (in absence of the escape box). For each habituation trial, an animal was placed onto the center of the elevated platform and allowed to move freely over the platform for 4 min before the animal was returned to its home cage. Animals were then subjected to eight learning trials with visual cues around the platform and an escape box under one hole. The elevated platform was brightly illuminated as aversive stimulus. For each learning trial, we placed an animal onto the center of the platform and allowed it to move freely for 4 min. We recorded the latency of animals to locate and enter the escape box. In the case an animal failed to enter the escape box during a 4 min trial period, we gently coaxed the animal into the escape box, allowing the animal to stay in the box for 2 min before returning it to its home cage. Probe trials to assess memory retrieval were conducted in presence of original visual cues, but in absence of escape box. Animals were placed onto the center of the platform and movements were observed for 2 min to identify the latency for animals to touch the original escape hole. We also divided the platform into four equal quadrants and identified the percentage of time over the 2 min period that animals spent within the target quadrant containing the escape hole.

Bulk RNA sequencing

RNA-sequencing was performed using total RNAs isolated from freshly dissected brain tissues using the RNeasy Mini Plus kit (Qiagen). TruSeq stranded cDNA libraries and 100-nucleotide paired reads with the Illumina Novaseq6000 S4 system were generated at Psomagen, Inc.. Sequencing reads were aligned to a customized mouse reference genome mm10 using STAR aligner v2.5.3a[71] guided by a customized mouse GENCODE gene model release v15. Here, the customized mouse reference genome sequence file was prepared based on the mm10 sequence by inserting 3 pseudo chromosomes, containing human APP, PSEN1, or MAPT gene sequences, respectively. Meanwhile, the GENCODE gene annotation GTF file was customized by adding annotations corresponding to human APP, PSEN1, and MAPT transgenes so that the expression of human APP/PSEN1/MAPT genes in the transgenic mice could be quantified. Mapped reads were summarized to gene levels using the featureCounts program v1.6.3[72]. Raw count data were normalized by the voom function in the R limma package[73] and then differential expression was called between sample conditions by the moderated t-test implemented in limma. Differentially expressed genes (DEGs) were defined to have at least 1.2-fold change in expression and Benjamini-Hochberg (BH) (Benjamini and Hochberg, 1995) adjusted $P \leq 0.05$.

Single-cell sequencing

scRNA-seq was performed using the 10X Genomics system at the Mount Sinai Genomics core facility. To prepare single cell suspensions for library preparation, fresh brain tissues were dissociated using a Papain neural tissue dissociation kit (Miltenyi 130-092-628). One mouse was used for each genotype condition. The scRNA-seq data were analyzed using the Seurat package[68]. Starting from Cell Ranger derived unique molecular identifier (UMI) count matrices, quality control (QC) was first performed by removing cells with either too few genes (≤ 200), too many genes (≥ 5000), an excessive number of UMI counts (≥ 50,000), or more than 10% mitochondrial reads, retaining 27,286 cells after filtering. Meanwhile, insufficiently detected genes were removed by keeping 18,762 genes expressed in more than two cells. After QC, we utilized Seurat's canonical correlation analysis (CCA) pipeline to integrate data across sample conditions. Next, dimensional reduction was performed using principal component analysis (PCA). The significant principal components explaining more than 90% of variance were selected for cell clustering using Seurat's graph-based clustering approach. We projected the normalized dataset onto a 2D space determined by Uniform Manifold Approximation and Projection for Dimension Reduction (UMAP)[74]. For each cluster, we calculated cluster gene signatures by comparing cells in one cluster against cells of remaining clusters using Wilcox rank sum test. Next, we interrogated the expression patterns of known marker genes to associate clusters with major cell-types: neurons (*Gad1*, *Slc17a7*), astrocytes (*Aqp4*), oligodendrocytes (*Mog*), microglia (*Tmem119*, *Trem2*, and *Tyrobp*), oligodendrocyte progenitor cells (*Vcan*), endothelial cells (*Flt1*), and pericytes (*Ambp*). To identify subclusters of astrocytes or microglia, cells from the astrocyte or microglia clusters defined above were extracted as subset. Then dimensional reduction was again performed using PCA, with the top principal components selected for cell clustering by Seurat's graph-based clustering approach. Signature score profiling for reactive astrocyte signatures was calculated using gene lists derived from the literature[10, 42, 43] (Table S2).

Database analyses

Analysis of the expression of Plexin-B1 in cell types of the CNS was performed using Brain RNA-seq platform (www.brainrnaseq.org)[31, 32]. The enrichment of Plexin-B1 network genes was performed against CNS cell type marker genes (defined in ref.[75]) and the MSigDB signature database[76, 77] with Fisher exact test.

Gene ontology enrichment analysis for sets of differentially expressed genes (cutoff: 1.25 fold change) was performed with the Enrichr platform[78] (maayanlab.cloud/Enrichr/).

We ran cell-cell communication analysis between the cell type pairs using CellphoneDB (v4.0.0)[45] for each sample separately. CellphoneDB first calculated the mean of the ligand and receptor expression in the interacting clusters. To estimate the *P* value significance of the mean expression, an empirical shuffling approach randomly permuting the cluster labels of all cells was employed by CellphoneDB to estimate a null distribution of the mean of the ligand and receptor expression. The *P* value for the likelihood of cell-type specificity of a given receptor–ligand complex was calculated as the proportion of the permuted means that were as high as or higher than the observed mean.

Statistical analysis

Statistical analyses were performed with GraphPad Prism 10 software, with the setting NEJM (New England Journal of Medicine) for reporting of *P* values. Bar graph data are presented as mean ± SEM.

Supplementary Material

Refer to Web version on PubMed Central for supplementary material.

Acknowledgements

This research project was supported by the National Institute of Aging (NIH-NIA) grants U01AG046170 and RF1AG057440, and New York State DOH grant SCIRB C39068GG. We thank Dr. Michelle Ehrlich at Icahn School of Medicine at Mount Sinai for advice and sharing AD mice. We also thank Dr. Jia Liu at the CUNY Epigenetics Core Facility for expert advice for RNAscope studies and the Mount Sinai microscopy core team for support in confocal imaging.

Data availability

The human postmortem sequencing data are available via the AD Knowledge Portal (https://adknowledgeportal.synapse.org). The AD Knowledge Portal is a platform for accessing data, analyses, and tools generated by the Accelerating Medicines Partnership (AMP-AD) Target Discovery Program and other National Institute on Aging (NIA)-supported programs to enable open-science practices and accelerate translational learning. The data, analyses, and tools are shared early in the research cycle without a publication embargo on a secondary use. Data is available for general research use according to the following requirements for data access and data attribution (https://adknowledgeportal.synapse.org/DataAccess/Instructions).

Both bulk and single cell RNA-seq data sets generated by this study have been deposited at the AMP-AD knowledge portal under Synapse ID syn26076735 (https://www.synapse.org/#!Synapse:syn26076735).

References

1. Long JM & Holtzman DM Alzheimer Disease: An Update on Pathobiology and Treatment Strategies. Cell 179, 312–339 (2019). [PubMed: 31564456]
2. Gandy S & DeKosky ST Toward the treatment and prevention of Alzheimer's disease: rational strategies and recent progress. Annu Rev Med 64, 367–383 (2013). [PubMed: 23327526]
3. Gandy S & Ehrlich ME Alzheimer mutant speeds APP transport. J Exp Med 218 (2021).
4. Matejuk A & Ransohoff RM Crosstalk Between Astrocytes and Microglia: An Overview. Front Immunol 11, 1416 (2020). [PubMed: 32765501]
5. Leng F & Edison P Neuroinflammation and microglial activation in Alzheimer disease: where do we go from here? Nat Rev Neurol 17, 157–172 (2021). [PubMed: 33318676]
6. Yuan P, et al. TREM2 Haplodeficiency in Mice and Humans Impairs the Microglia Barrier Function Leading to Decreased Amyloid Compaction and Severe Axonal Dystrophy. Neuron 92, 252–264 (2016). [PubMed: 27710785]
7. Condello C, Yuan P, Schain A & Grutzendler J Microglia constitute a barrier that prevents neurotoxic protofibrillar Aβ42 hotspots around plaques. Nat Commun 6, 6176 (2015). [PubMed: 25630253]
8. Smit T, et al. Reactive astrocytes as treatment targets in Alzheimer's disease-Systematic review of studies using the APPswePS1dE9 mouse model. Glia 69, 1852–1881 (2021). [PubMed: 33634529]
9. Bouvier DS, et al. High Resolution Dissection of Reactive Glial Nets in Alzheimer's Disease. Sci Rep 6, 24544 (2016). [PubMed: 27090093]
10. Liddelow SA, et al. Neurotoxic reactive astrocytes are induced by activated microglia. Nature 541, 481–487 (2017). [PubMed: 28099414]
11. Zhang B, et al. Integrated systems approach identifies genetic nodes and networks in late-onset Alzheimer's disease. Cell 153, 707–720 (2013). [PubMed: 23622250]
12. Wang M, et al. Transformative Network Modeling of Multi-omics Data Reveals Detailed Circuits, Key Regulators, and Potential Therapeutics for Alzheimer's Disease. Neuron 109, 257–272.e214 (2021). [PubMed: 33238137]
13. Wang M, et al. The Mount Sinai cohort of large-scale genomic, transcriptomic and proteomic data in Alzheimer's disease. Sci Data 5, 180185 (2018). [PubMed: 30204156]
14. Tran TS, Kolodkin AL & Bharadwaj R Semaphorin regulation of cellular morphology. Annu Rev Cell Dev Biol 23, 263–292 (2007). [PubMed: 17539753]
15. Jongbloets BC & Pasterkamp RJ Semaphorin signalling during development. Development 141, 3292–3297 (2014). [PubMed: 25139851]
16. Koropouli E & Kolodkin AL Semaphorins and the dynamic regulation of synapse assembly, refinement, and function. Curr Opin Neurobiol 27, 1–7 (2014). [PubMed: 24598309]
17. Gurrapu S & Tamagnone L Transmembrane semaphorins: Multimodal signaling cues in development and cancer. Cell Adh Migr 10, 675–691 (2016). [PubMed: 27295627]
18. Hota PK & Buck M Plexin structures are coming: opportunities for multilevel investigations of semaphorin guidance receptors, their cell signaling mechanisms, and functions. Cell Mol Life Sci 69, 3765–3805 (2012). [PubMed: 22744749]
19. Junqueira Alves C, et al. Evolution and Diversity of Semaphorins and Plexins in Choanoflagellates. Genome Biol Evol 13 (2021).
20. Junqueira Alves C, Yotoko K, Zou H & Friedel RH Origin and evolution of plexins, semaphorins, and Met receptor tyrosine kinases. Sci Rep 9, 1970 (2019). [PubMed: 30760850]
21. Deng S, et al. Plexin-B2, but not Plexin-B1, critically modulates neuronal migration and patterning of the developing nervous system in vivo. J Neurosci 27, 6333–6347 (2007). [PubMed: 17554007]

22. Fazzari P, et al. Plexin-B1 plays a redundant role during mouse development and in tumour angiogenesis. BMC Dev Biol 7, 55 (2007). [PubMed: 17519029]
23. Okuno T, et al. Roles of Sema4D-Plexin-B1 Interactions in the Central Nervous System for Pathogenesis of Experimental Autoimmune Encephalomyelitis. J Immunol 184, 1499–1506 (2010). [PubMed: 20038643]
24. Takamatsu H, et al. Semaphorins guide the entry of dendritic cells into the lymphatics by activating myosin II. Nat Immunol 11, 594–600 (2010). [PubMed: 20512151]
25. Negishi-Koga T, et al. Suppression of bone formation by osteoclastic expression of semaphorin 4D. Nat Med 17, 1473–1480 (2011). [PubMed: 22019888]
26. Mostafavi S, et al. A molecular network of the aging human brain provides insights into the pathology and cognitive decline of Alzheimer's disease. Nat Neurosci 21, 811–819 (2018). [PubMed: 29802388]
27. Yu L, et al. Targeted brain proteomics uncover multiple pathways to Alzheimer's dementia. Ann Neurol 84, 78–88 (2018). [PubMed: 29908079]
28. Mathys H, et al. Single-cell transcriptomic analysis of Alzheimer's disease. Nature 570, 332–337 (2019). [PubMed: 31042697]
29. Bos JL From Ras to Rap and Back, a Journey of 35 Years. Cold Spring Harb Perspect Med 8 (2018).
30. Neff RA, et al. Molecular subtyping of Alzheimer's disease using RNA sequencing data reveals novel mechanisms and targets. Sci Adv 7 (2021).
31. Zhang Y, et al. Purification and Characterization of Progenitor and Mature Human Astrocytes Reveals Transcriptional and Functional Differences with Mouse. Neuron 89, 37–53 (2016). [PubMed: 26687838]
32. Zhang Y, et al. An RNA-sequencing transcriptome and splicing database of glia, neurons, and vascular cells of the cerebral cortex. J Neurosci 34, 11929–11947 (2014). [PubMed: 25186741]
33. Zhou Y, et al. Human and mouse single-nucleus transcriptomics reveal TREM2-dependent and TREM2-independent cellular responses in Alzheimer's disease. Nat Med 26, 131–142 (2020). [PubMed: 31932797]
34. Jankowsky JL, et al. Mutant presenilins specifically elevate the levels of the 42 residue beta-amyloid peptide in vivo: evidence for augmentation of a 42-specific gamma secretase. Hum Mol Genet 13, 159–170 (2004). [PubMed: 14645205]
35. Sakers K, et al. Astrocytes locally translate transcripts in their peripheral processes. Proc Natl Acad Sci U S A 114, E3830–E3838 (2017). [PubMed: 28439016]
36. Boulay AC, et al. Translation in astrocyte distal processes sets molecular heterogeneity at the gliovascular interface. Cell Discov 3, 17005 (2017). [PubMed: 28377822]
37. Daviaud N, Chen K, Huang Y, Friedel RH & Zou H Impaired cortical neurogenesis in plexin-B1 and -B2 double deletion mutant. Dev Neurobiol 76, 882–899 (2016). [PubMed: 26579598]
38. Friedel RH, et al. Gene targeting using a promoterless gene trap vector ("targeted trapping") is an efficient method to mutate a large fraction of genes. Proc Natl Acad Sci U S A 102, 13188–13193 (2005). [PubMed: 16129827]
39. Hyman BT, et al. National Institute on Aging-Alzheimer's Association guidelines for the neuropathologic assessment of Alzheimer's disease. Alzheimers Dement 8, 1–13 (2012). [PubMed: 22265587]
40. Montine TJ, et al. National Institute on Aging-Alzheimer's Association guidelines for the neuropathologic assessment of Alzheimer's disease: a practical approach. Acta Neuropathol 123, 1–11 (2012). [PubMed: 22101365]
41. Bakken TE, et al. Single-nucleus and single-cell transcriptomes compared in matched cortical cell types. PLoS One 13, e0209648 (2018). [PubMed: 30586455]
42. Habib N, et al. Disease-associated astrocytes in Alzheimer's disease and aging. Nat Neurosci 23, 701–706 (2020). [PubMed: 32341542]
43. Burda JE, et al. Divergent transcriptional regulation of astrocyte reactivity across disorders. Nature 606, 557–564 (2022). [PubMed: 35614216]

44. Keren-Shaul H, et al. A Unique Microglia Type Associated with Restricting Development of Alzheimer’s Disease. Cell 169, 1276–1290.e1217 (2017). [PubMed: 28602351]

45. Garcia-Alonso L, et al. Single-cell roadmap of human gonadal development. Nature 607, 540–547 (2022). [PubMed: 35794482]

46. Sun W, et al. SOX9 Is an Astrocyte-Specific Nuclear Marker in the Adult Brain Outside the Neurogenic Regions. J Neurosci 37, 4493–4507 (2017). [PubMed: 28336567]

47. Stanley ER & Chitu V CSF-1 receptor signaling in myeloid cells. Cold Spring Harb Perspect Biol 6 (2014).

48. Lee SJ, et al. ICAM-1-induced expression of proinflammatory cytokines in astrocytes: involvement of extracellular signal-regulated kinase and p38 mitogen-activated protein kinase pathways. J Immunol 165, 4658–4666 (2000). [PubMed: 11035109]

49. Kutz SM, Higgins CE & Higgins PJ Novel Combinatorial Therapeutic Targeting of PAI-1 (SERPINE1) Gene Expression in Alzheimer’s Disease. Mol Med Ther 1, 106 (2012). [PubMed: 23847772]

50. McGrath ER, et al. Circulating IGFBP-2: a novel biomarker for incident dementia. Ann Clin Transl Neurol 6, 1659–1670 (2019). [PubMed: 31373442]

51. Canals I, et al. Rapid and efficient induction of functional astrocytes from human pluripotent stem cells. Nat Methods 15, 693–696 (2018). [PubMed: 30127505]

52. Huang Y, et al. Microglia use TAM receptors to detect and engulf amyloid β plaques. Nat Immunol 22, 586–594 (2021). [PubMed: 33859405]

53. Condello C, Schain A & Grutzendler J Multicolor time-stamp reveals the dynamics and toxicity of amyloid deposition. Sci Rep 1, 19 (2011). [PubMed: 22355538]

54. Gowrishankar S, et al. Massive accumulation of luminal protease-deficient axonal lysosomes at Alzheimer’s disease amyloid plaques. Proc Natl Acad Sci U S A 112, E3699–3708 (2015). [PubMed: 26124111]

55. Sharoar MG, Hu X, Ma XM, Zhu X & Yan R Sequential formation of different layers of dystrophic neurites in Alzheimer’s brains. Mol Psychiatry 24, 1369–1382 (2019). [PubMed: 30899091]

56. Chistiakov DA, Killingsworth MC, Myasoedova VA, Orekhov AN & Bobryshev YV CD68/macrosialin: not just a histochemical marker. Lab Invest 97, 4–13 (2017).

57. Lemke G & Huang Y The dense-core plaques of Alzheimer’s disease are granulomas. J Exp Med 219 (2022).

58. Deb Roy A, et al. Optogenetic activation of Plexin-B1 reveals contact repulsion between osteoclasts and osteoblasts. Nat Commun 8, 15831 (2017). [PubMed: 28635959]

59. Zhou X, et al. Microglia and macrophages promote corralling, wound compaction and recovery after spinal cord injury via Plexin-B2. Nat Neurosci 23, 337–350 (2020). [PubMed: 32112058]

60. Zhou Y, Gunput RA & Pasterkamp RJ Semaphorin signaling: progress made and promises ahead. Trends Biochem Sci 33, 161–170 (2008). [PubMed: 18374575]

61. Clark IC, et al. Barcoded viral tracing of single-cell interactions in central nervous system inflammation. Science 372 (2021).

62. Mehta V, et al. The guidance receptor plexin D1 is a mechanosensor in endothelial cells. Nature 578, 290–295 (2020). [PubMed: 32025034]

63. Evans EE, et al. Evidence that semaphorin 4D is upregulated in neurons in Huntington’s and Alzheimer’s diseases: Effects of a SEMA4D blocking antibody on FDG-PET in a clinical trial, and treatment rationale for its use in AD. Alzheimer’s & Dementia 16, e043971 (2020).

64. Cowan R, et al. Nanobody inhibitors of Plexin-B1 identify allostery in plexin-semaphorin interactions and signaling. J Biol Chem 299, 104740 (2023). [PubMed: 37088134]

65. Matsunaga Y, Bashiruddin NK, Kitago Y, Takagi J & Suga H Allosteric Inhibition of a Semaphorin 4D Receptor Plexin B1 by a High-Affinity Macrocyclic Peptide. Cell Chem Biol 23, 1341–1350 (2016). [PubMed: 27984026]

66. Zhu J, et al. Increasing the Power to Detect Causal Associations by Combining Genotypic and Expression Data in Segregating Populations. PLoS Comput Biol 3, e69 (2007). [PubMed: 17432931]

67. Zhu J, et al. Stitching together multiple data dimensions reveals interacting metabolomic and transcriptomic networks that modulate cell regulation. PLoS Biol 10, e1001301 (2012). [PubMed: 22509135]
68. Stuart T, et al. Comprehensive Integration of Single-Cell Data. Cell 177, 1888–1902.e1821 (2019). [PubMed: 31178118]
69. Korsunsky I, et al. Fast, sensitive and accurate integration of single-cell data with Harmony. Nature Methods 16, 1289–1296 (2019). [PubMed: 31740819]
70. Gawel K, Gibula E, Marszalek-Grabska M, Filarowska J & Kotlinska JH Assessment of spatial learning and memory in the Barnes maze task in rodents-methodological consideration. Naunyn Schmiedebergs Arch Pharmacol 392, 1–18 (2019).
71. Dobin A, et al. STAR: ultrafast universal RNA-seq aligner. Bioinformatics 29, 15–21 (2013). [PubMed: 23104886]
72. Liao Y, Smyth GK & Shi W featureCounts: an efficient general purpose program for assigning sequence reads to genomic features. Bioinformatics 30, 923–930 (2014). [PubMed: 24227677]
73. Ritchie ME, et al. limma powers differential expression analyses for RNA-sequencing and microarray studies. Nucleic Acids Res 43, e47 (2015). [PubMed: 25605792]
74. McInnes L, Healy J & Melville J UMAP: Uniform Manifold Approximation and Projection for Dimension Reduction. arXiv 1802.03426 (2018).
75. McKenzie AT, et al. Brain Cell Type Specific Gene Expression and Co-expression Network Architectures. Scientific reports 8, 8868 (2018). [PubMed: 29892006]
76. Liberzon A, et al. The Molecular Signatures Database (MSigDB) hallmark gene set collection. Cell systems 1, 417–425 (2015). [PubMed: 26771021]
77. Subramanian A, et al. Gene set enrichment analysis: a knowledge-based approach for interpreting genome-wide expression profiles. Proc Natl Acad Sci U S A 102, 15545–15550 (2005). [PubMed: 16199517]
78. Xie Z, et al. Gene Set Knowledge Discovery with Enrichr. Curr Protoc 1, e90 (2021). [PubMed: 33780170]

Figure Legends References

1. Haroutunian V, Katsel P & Schmeidler J Transcriptional vulnerability of brain regions in Alzheimer's disease and dementia. Neurobiol Aging 30, 561–573 (2009). [PubMed: 17845826]
2. Neff RA, et al. Molecular subtyping of Alzheimer's disease using RNA sequencing data reveals novel mechanisms and targets. Sci Adv 7 (2021).
3. Zhang Y, et al. An RNA-sequencing transcriptome and splicing database of glia, neurons, and vascular cells of the cerebral cortex. J Neurosci 34, 11929–11947 (2014). [PubMed: 25186741]
4. Zhang Y, et al. Purification and Characterization of Progenitor and Mature Human Astrocytes Reveals Transcriptional and Functional Differences with Mouse. Neuron 89, 37–53 (2016). [PubMed: 26687838]
5. Mathys H, et al. Single-cell transcriptomic analysis of Alzheimer's disease. Nature 570, 332–337 (2019). [PubMed: 31042697]
6. Zhou Y, et al. Human and mouse single-nucleus transcriptomics reveal TREM2-dependent and TREM2-independent cellular responses in Alzheimer's disease. Nat Med 26, 131–142 (2020). [PubMed: 31932797]
7. Hyman BT, et al. National Institute on Aging-Alzheimer's Association guidelines for the neuropathologic assessment of Alzheimer's disease. Alzheimers Dement 8, 1–13 (2012). [PubMed: 22265587]
8. Montine TJ, et al. National Institute on Aging-Alzheimer's Association guidelines for the neuropathologic assessment of Alzheimer's disease: a practical approach. Acta Neuropathol 123, 1–11 (2012). [PubMed: 22101365]
9. Keren-Shaul H, et al. A Unique Microglia Type Associated with Restricting Development of Alzheimer's Disease. Cell 169, 1276–1290.e1217 (2017). [PubMed: 28602351]

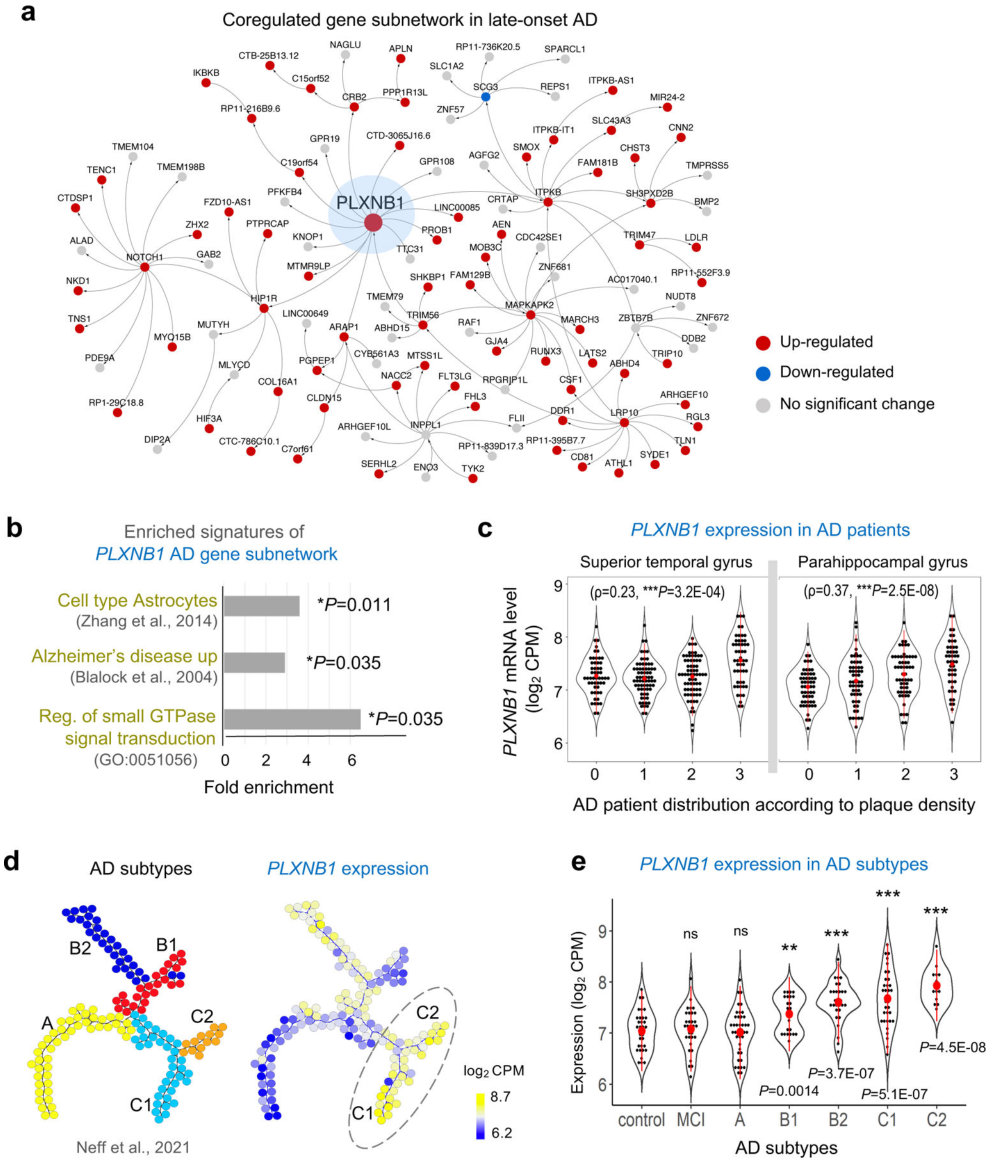

Figure 1. Plexin-B1 is a hub gene of AD gene subnetwork with expression correlating with AD pathology.

A) Multiscale gene network analysis of multi-omics AD patient data (Mount Sinai Brain Bank cohort) identified *PLXNB1* as a hub in a coregulated gene subnetwork underlying late-onset AD.

B) Significantly enriched gene sets in the *PLXNB1* subnetwork.

C) *PLXNB1* mRNA levels positively correlated with plaque density in the brain regions affected by AD (Spearman's Rho (ρ) rank correlation analyses; data from Mount Sinai Brain Bank cohort). Each dot represents one patient sample. AD patients were classified according to mean plaque density as described in ref.[1]

D) *PLXNB1* mRNA is up-regulated in AD patient samples, especially those with greater Aβ-associated alterations (i.e., AD subtypes C1 and C2), as defined in ref.[2]. Each circle represents one patient from Mount Sinai Brain Bank cohort (n=151 patients).

E) *PLXNB1* expression in parahippocampal gyrus of health controls, patients with mild cognitive impairment (MCI), or different AD subtypes (as defined in ref.[2]). Each dot represents one patient. One-tailed *t*-test.

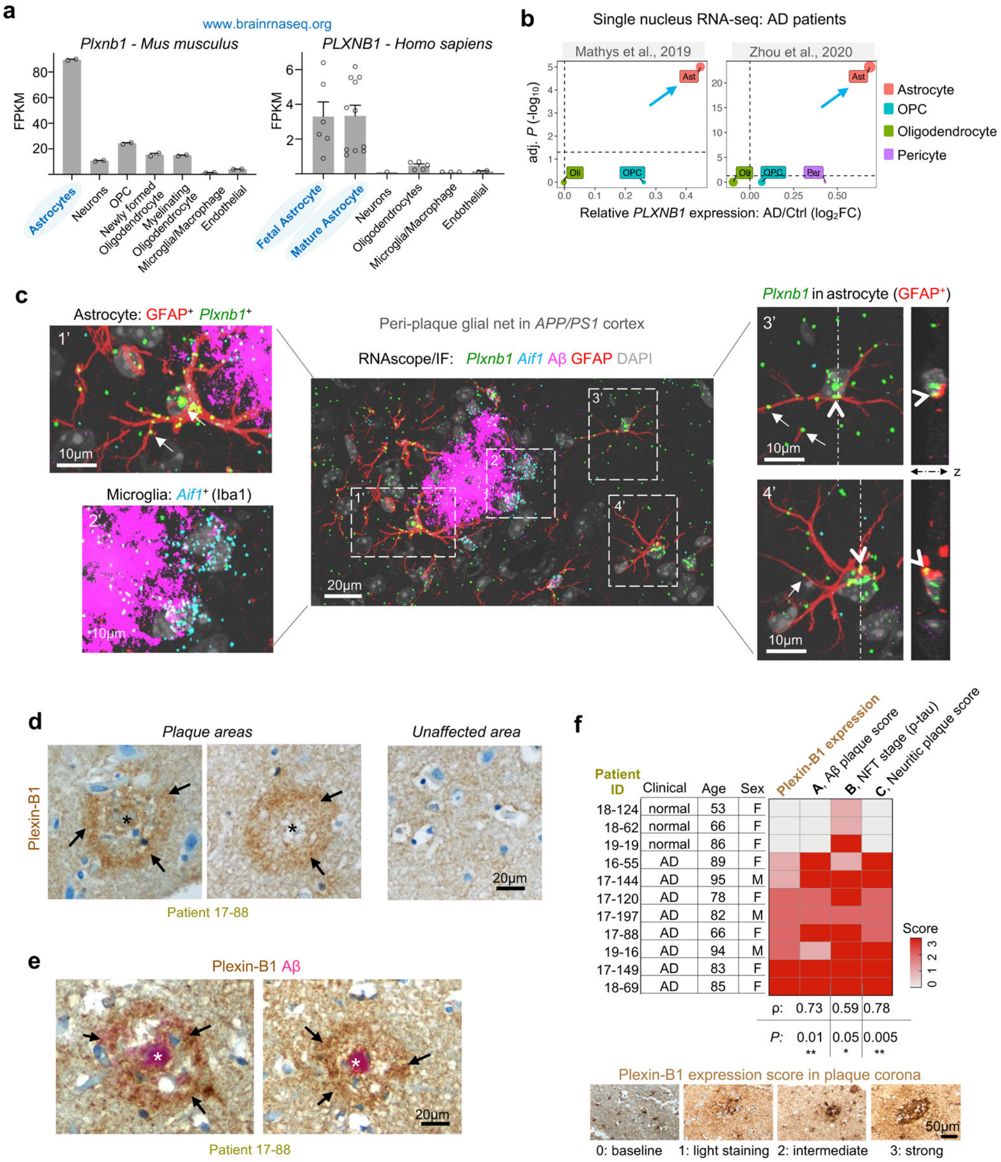

Patient ID	Clinical	Age	Sex
18-124	normal	53	F
18-62	normal	66	F
19-19	normal	86	F
16-55	AD	89	F
17-144	AD	95	M
17-120	AD	78	F
17-197	AD	82	M
17-88	AD	66	F
19-16	AD	94	M
17-149	AD	83	F
18-69	AD	85	F

	A	B	C
ρ:	0.73	0.59	0.78
P:	0.01 **	0.05 *	0.005 **

Figure 2. Upregulation of Plexin-B1 in peri-plaque astrocytes in AD.

A) Transcriptomic data show a predominant expression of Plexin-B1 in astrocytes in both mouse and human brain. Graphs compiled from brainrnaseq.org database (refs.[3, 4]).

B) Analysis of snRNA-seq data of human AD patients from two independent studies (refs.[5, 6]) revealed significant upregulation of *PLXNB1* in astrocytes (arrows), but not other cell types. Horizontal dashed lines denote significance threshold of P=0.05 (Bonferroni corrected). Node sizes are proportional to *PLXNB1* mean expression levels in different cell types.

C) RNAscope ISH for *Plxnb1* and *Aif1* (encoding Iba1) mRNAs combined with IF for GFAP and Aβ (antibody 6E10) of cortex of 6 months old *APP/PS1* mouse. DAPI for nuclear staining. Note the presence of *Plxnb1* mRNA puncta (examples denoted by arrows) in peri-plaque astrocytes (GFAP$^+$) (enlarged images 1’, 3’, and 4’), but not microglia (enlarged image 2’). Orthogonal slices of z-stacks of areas 3’ and 4’ confirmed localization of *Plxnb1* mRNA puncta inside soma and branches of astrocytes (arrowheads).

D, E) IHC images of post-mortem AD patient brain probed for Plexin-B1 alone (D) or co-stained for β-amyloid (antibody 4G8) (E). Hematoxylin for nuclear counterstain. Note elevated Plexin-B1 protein expression in a corona-like pattern (arrows) surrounding amyloid plaques.

F) Heatmap of Plexin-B1 protein expression score near plaques and corresponding neuropathology scores for 11 AD patients (Mount Sinai Brain Bank cohort). Neuropathology scoring according to “ABC” system[7, 8]. Pearson correlation coefficient (ρ) and associated *P* values are indicated. Representative examples of Plexin-B1 expression score scheme shown below.

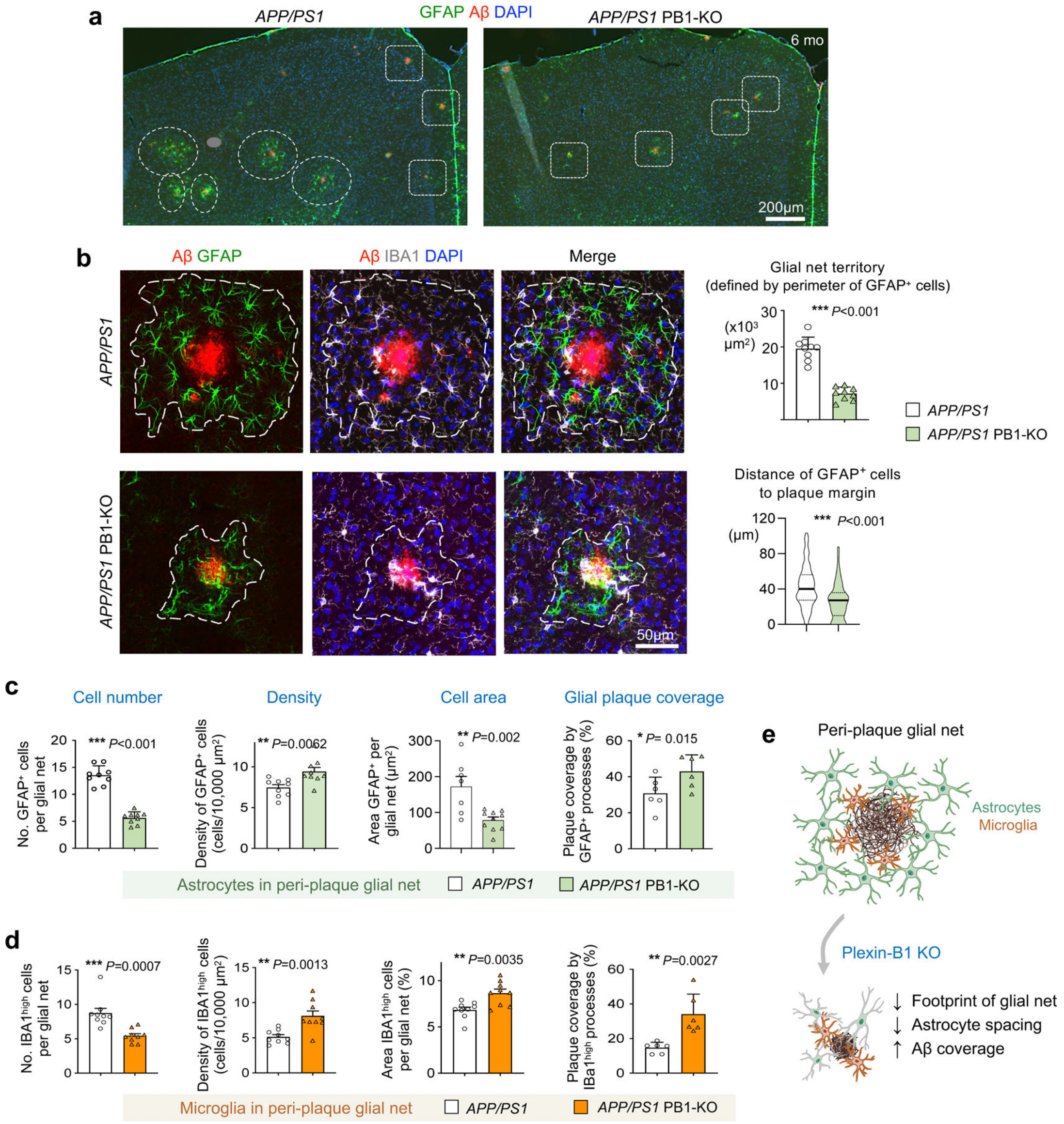

Figure 3. Plexin-B1 KO reduced the footprint of peri-plaque glial nets in mouse AD model.

A) Representative IF images of cortical areas stained for Aβ (antibody 6E10), reactive astrocytes (GFAP), and nuclear counterstaining (DAPI). Note smaller glial nets around amyloid plaques (dashed boxes) in *APP/PS1* PB1-KO mice as compared to the larger ones (dashed ovals) in *APP/PS1* mice. A small gray oval in *APP/PS1* image covers a dust artifact. **B)** Confocal IF images of glial nets surrounding plaques in *APP/PS1* and *APP/PS1* PB1-KO mice. Dashed lines outline the perimeter of glial net territory defined by GFAP$^+$ cells. Quantifications show reduced glial net sizes in PB1-KO mice, with reduced distances of GFAP$^+$ cells to plaque. Unpaired *t*-test. n=9 sections per genotype, from 3 independent mice each; for glial net size, each data point represents the mean of 11 randomly selected peri-plaque glia nets from one section; for cell distance to plaque, violin plots from n=104 and 55 cells for genotypes, showing median, quartiles, and minimum and maximum values.

C) Quantifications show lower number and reduced cell areas of GFAP$^+$ astrocytes in glial nets in *APP/PS1* PB1-KO mice. In contrast, density of GFAP$^+$ cells was higher in PB1-KO condition, as was plaque coverage by GFAP$^+$ astrocytic processes. Unpaired *t*-test. n=9 sections per genotype from 3 independent mice (each data point represents the mean of randomly selected glia nets from one section).

D) Quantifications of IBA1^{high} microglia indicate lower number, but higher density, cell area, and plaque coverage in *APP/PS1* PB1-KO mice. Unpaired *t*-test. n=9 sections from 3 independent mice of each genotype (each data point represents the mean of randomly selected glia nets from one section).

E) Schematic depiction of phenotypic differences of glial nets with Plexin-B1 KO in AD: smaller but more compact peri-plaque glial nets, with fewer reactive astrocytes and activated microglia, reduced cellular spacing, and increased plaque coverage by glial processes.

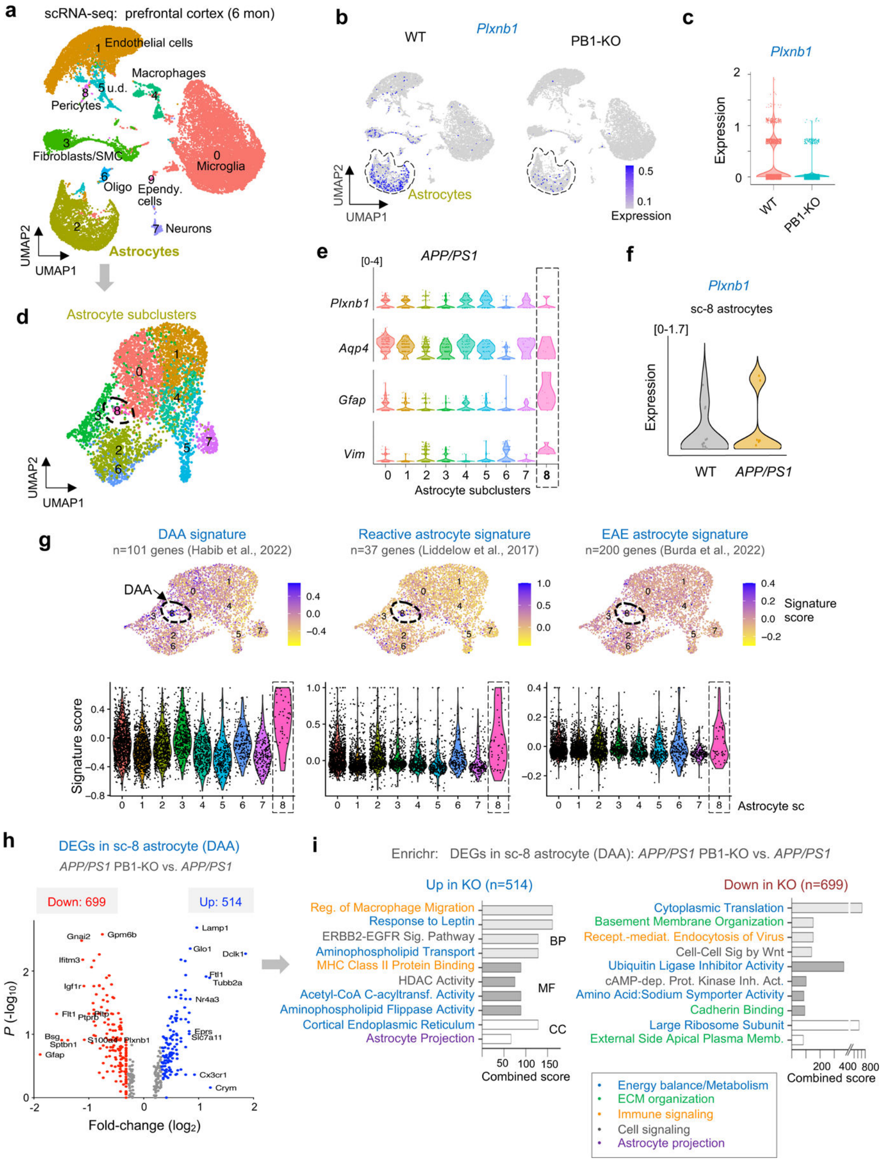

Figure 4. scRNA-seq reveals the impact of Plexin-B1 KO on activation profiles of reactive astrocytes in AD.

A) UMAP embedding of combined scRNA-seq data from prefrontal cortices of 6-month-old mice with genotypes WT, PB1-KO, *APP/PS1*, and *APP/PS1* PB1-KO. Ten major cell type clusters were detected. SMC, smooth muscle cells.

B, C) Feature and violin plots show a predominant expression of *Plxnb1* in astrocytes, and effective ablation in PB1-KO mice.

D) UMAP shows 9 astrocyte subclusters based on scRNA-seq data.

E) Expression of *Plxnb1* and marker genes in astrocyte subclusters in *APP/PS1* mice. Note higher expression of *Gfap* and *Vim* in sc-8.

F) Upregulation of *Plxnb1* mRNA in astrocyte subcluster sc-8 in *APP/PS1* mice as compared to WT.

G) Signature score profiling shows sc-8 with highest expression for gene signatures of disease associated astrocytes identified in AD (DAA), reactive astrocytes, and astrocytes in experimental autoimmune encephalomyelitis (EAE).

H) Volcano plot showing DEGs of sc-8 astrocytes, comparing *APP/PS1* PB1-KO vs. *APP/PS1* condition.

I) Gene ontology enrichment analysis by Enrichr of up- and downregulated DEGs in sc-8 astrocytes *(APP/PS1* PB1-KO vs. *APP/PS1*). BP, Biological process; MF, molecular function; CC, cellular component.

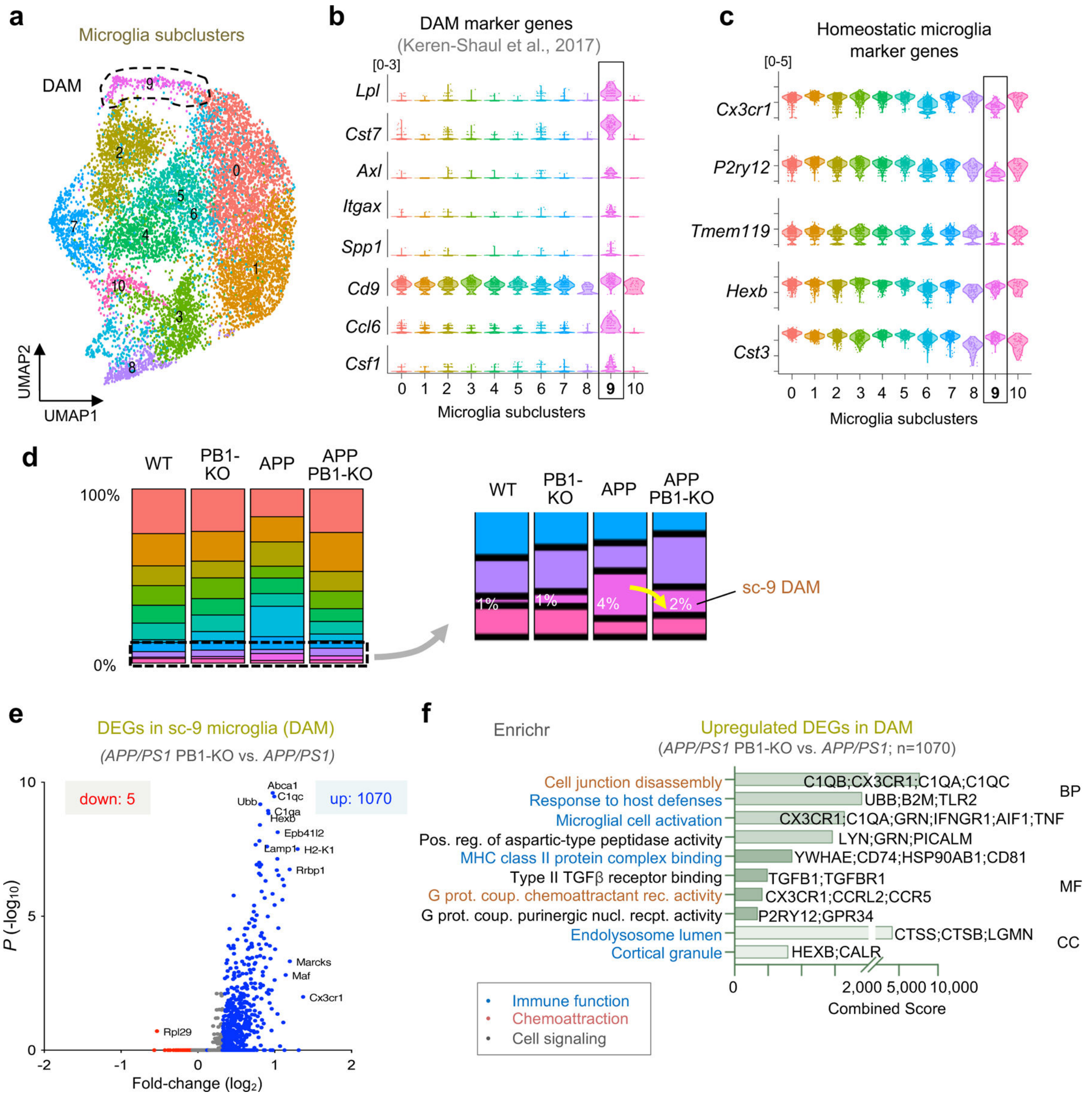

Figure 5. Increased microglial activation in *APP/PS1* PB1-KO mice.

A) UMAP embedding shows microglia subclusters, with sc-9 representing disease-associated microglia (DAM) as defined in ref.[9].

B) Violin plots show higher expression of DAM marker genes in microglia sc-9.

C) Violin plots show lower expression of homeostatic microglia genes *Cx3cr1*, *P2ry12*, and *Tmem119* in microglia sc-9.

D) Proportions of microglia subclusters in different genotype conditions. Microglia sc-9 (DAM-like) was expanded in *APP/PS1* mice, but this expansion was lowered in *APP/PS1* PB1-KO.

E) Volcano plot shows DEGs in DAM microglia sc-9 (*APP/PS1* PB1-KO vs. *APP/PS1*).

F) Gene ontology enrichment analysis by Enrichr of upregulated DEGs in microglia sc-9 (*APP/PS1* PB1-KO vs. *APP/PS1*) indicated increased microglial activation in Plexin-B1 deletion condition.

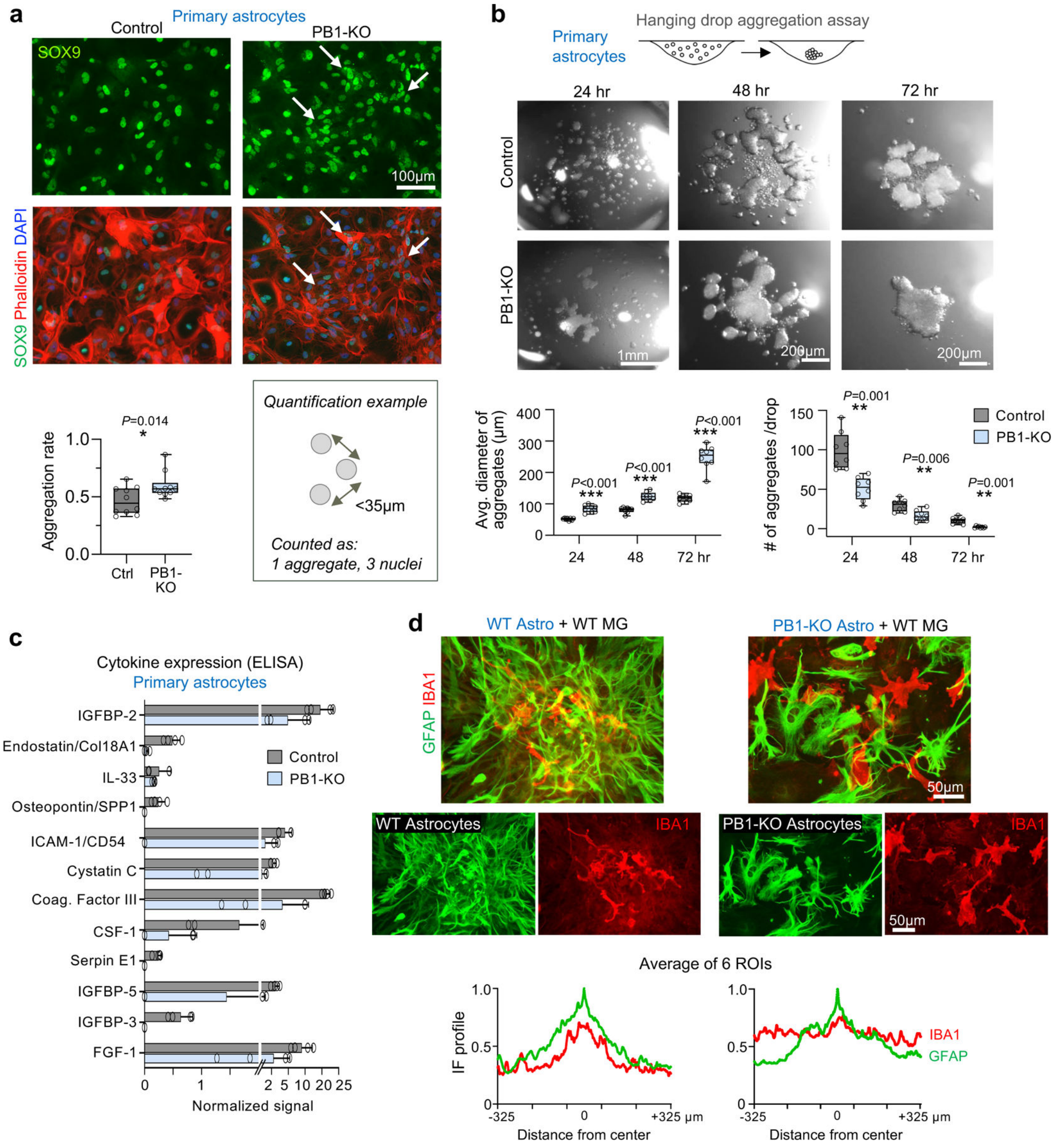

Figure 6. Plexin-B1 governs cell spacing/aggregation pattern and cytokine expression in primary astrocytes.

A) Primary astrocytes from control or PB1-KO mice were cultured for two days and stained for astrocyte nuclear marker Sox9 and F-actin (phalloidin). PB1-KO astrocytes displayed more clustering (arrows), defined as an inter-connected groups of cells with nuclei less than 35 μm apart. Aggregation rate defined as 1-(connected components/total nuclei). n=10 randomly selected areas from 4 independent experiments; unpaired *t*-test.

B) Images of control or PB1-KO astrocytes in hanging drop aggregation assay. PB1-KO astrocytes formed larger aggregates, resulting in lower total number of aggregates. n=8 drops for each condition from 3 independent experiments; two-way ANOVA with Sidak’s multiple comparison test.

C) Cytokine ELISA profiling (Proteome Profiler Mouse XL Cytokine Array, R&D Systems) revealed reduced cytokine/chemokine expression in PB1-KO astrocytes. n=4 four data points for each condition, from 2 independent assays.

D) IF images of 2 day co-culture of primary astrocytes with microglia, treated with TNFα (100 ng/ml) for 24 hr. In co-culture with WT astrocytes, microglia clustered together, a pattern absent in co-culture with PB1-KO astrocytes. Quantifications below show distribution of immunofluorescence (IF) profiles of GFAP and IBA1, averaged over 6 regions of interest (ROI).

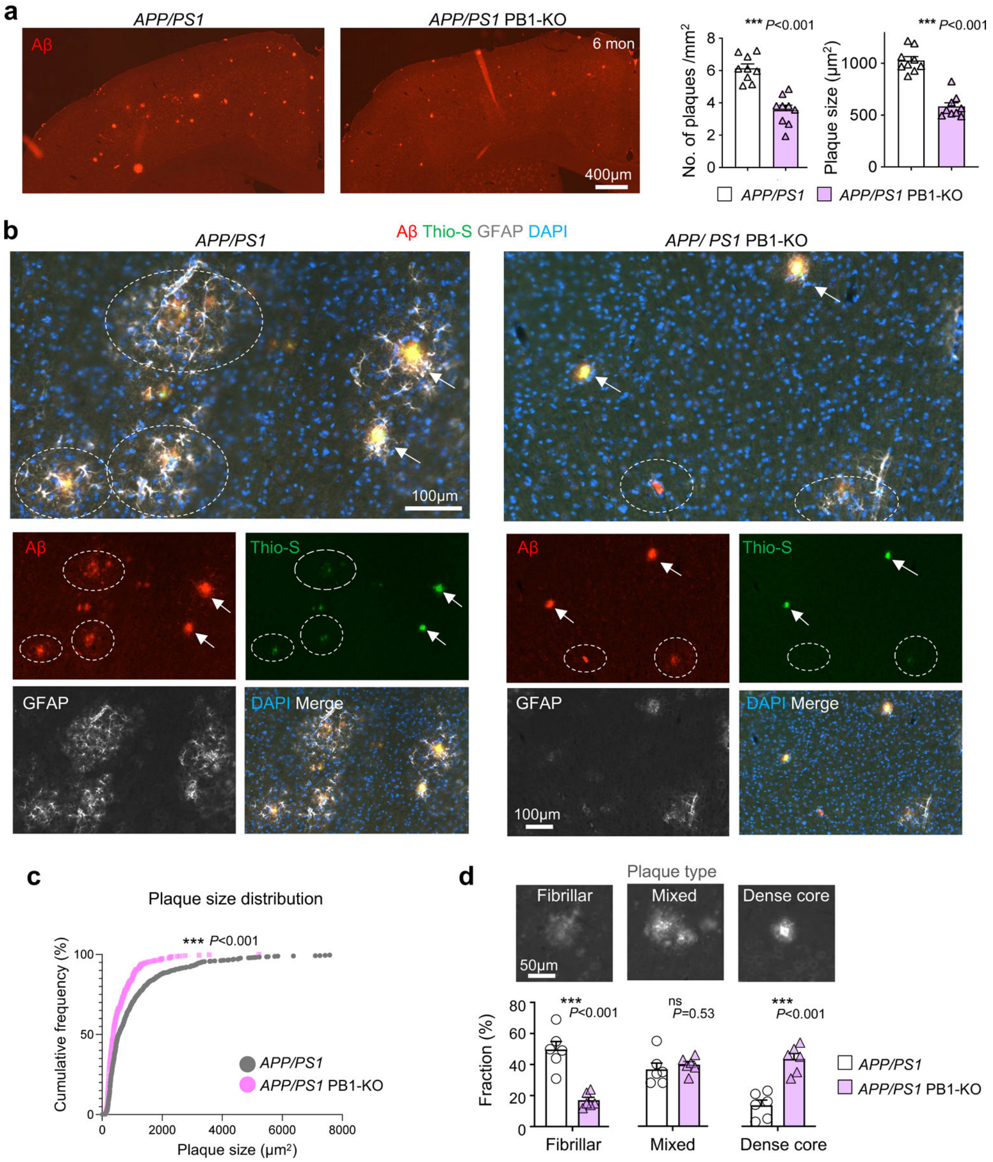

Figure 7. Reduced plaque burden and shift to dense-core type in AD mice with Plexin-B1 KO.

A) Representative IF images for amyloid plaques (antibody 6E10) in forebrain sections from 6-month-old *APP/PS1* mice with or without Plexin-B1 KO. Quantifications show reduced plaque burden (smaller number and size of plaques) with PB1-KO. Unpaired *t*-test. n=9 sections per genotype, from 3 independent mice each. For plaque size, each data point represents the mean of all plaques from one section.

B) IF images of forebrain sections show amyloid plaques in *APP/PS1* mice with and without PB1-KO. Dashed ovals denote diffuse plaques stained only weakly by the amyloid-binding Thio-S; arrows point to dense core plaques with strong staining by Thio-S. Note the reduced size of peri-plaque glial nets (demarcated by GFAP$^+$ cells) in PB1-KO.

C) Cumulative frequency plot shows more compact plaque areas (6E10 antibody staining) in Plexin-B1 KO mice. Two-way ANOVA with Sidak's multicomparison test. n=741 (*APP/*

PS1) and 428 (*APP/PS1* PB1-KO) plaques from 9 sections of three independent mice per genotype.

D) Quantification of plaque types shows that in *APP/PS1* mice, Plexin-B1 KO led to a shift of plaques from fibrillar to dense core type. Scoring scheme of plaques is illustrated above. n=6 brain sections per genotype. Unpaired *t*-test. ns, not significant.

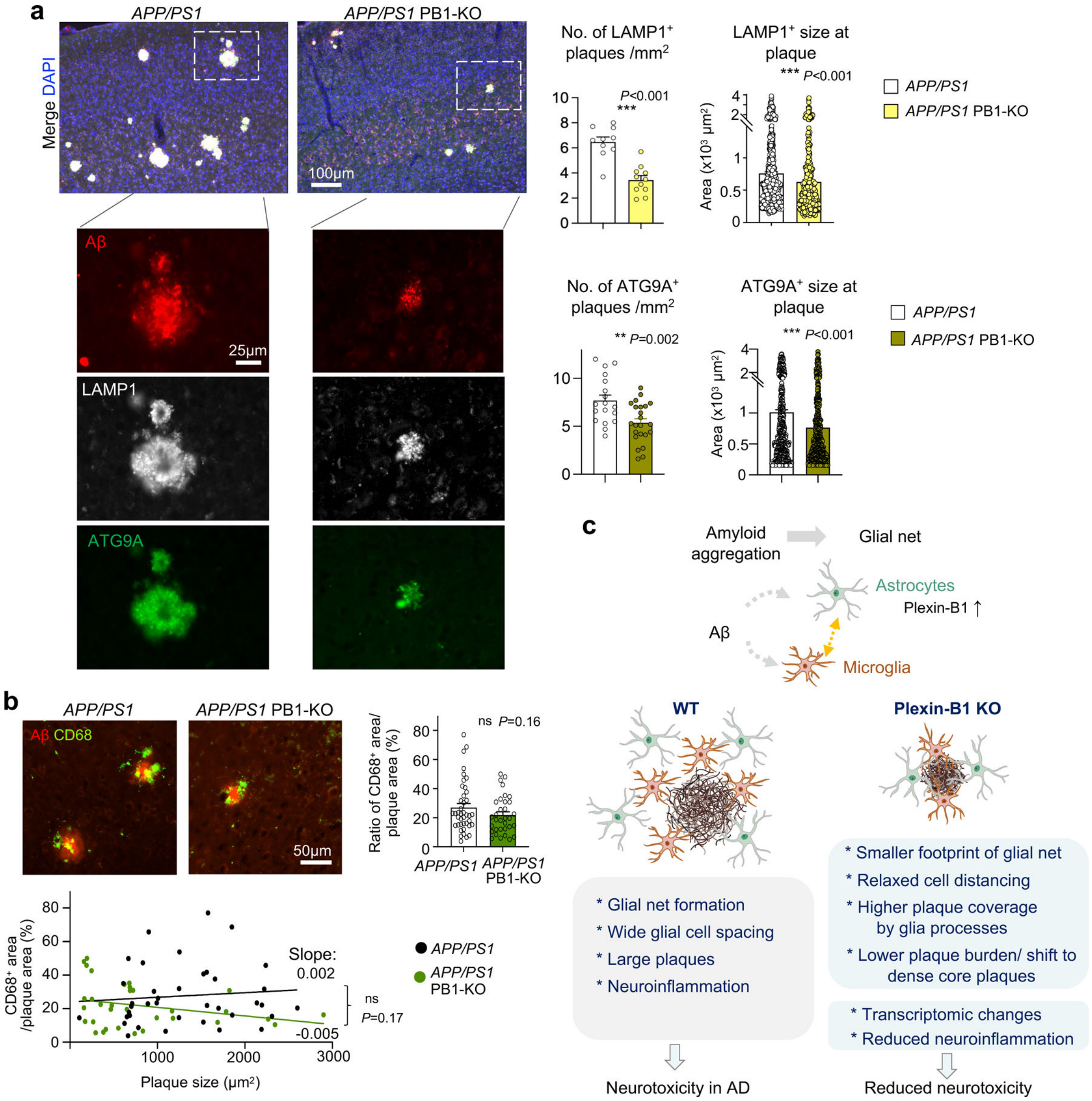

Figure 8. Decreased neuritic dystrophy in Plexin-B1 KO AD mice.

A) Representative IF images co-stained for amyloid plaque, neuritic dystrophy lysosomal marker LAMP1, and autophagosome marker ATG9A in forebrains of 6 months old *APP/PS1* and *APP/PS1* PB1-KO mice. Quantifications reveal reduced overall number and size of LAMP1 or ATG9A signals. Unpaired *t*-test. For number quantification, n=10–23 section areas from three independent mice per genotype. For LAMP$^+$ plaque size quantification, n= 623 (*APP/PS1*) or 364 (*APP/PS1* PB1-KO); for ATG9A$^+$ plaque size quantification, n= 715 (*APP/PS1*) or 540 (*APP/PS1* PB1-KO); three independent mice per genotype.

B) IF images of amyloid plaques surrounded by myeloid cells (stained for phagocytosis marker CD68). Quantifications show reduced CD68$^+$ signals around plaques, corresponding to smaller size of plaques in PB1-KO (note that the ratio of CD68$^+$ area in relation to plaque area was comparable between *APP/PS1* and *APP/PS1* PB1-KO). n=41 (*APP/PS1*) or 33 (*APP/PS1* PB1-KO) plaques, from 3 independent mice per genotype. For bar graph: Unpaired *t*-test. For dot plot: Simple linear regression test; ns, not significant.

C) Summary of protective effects of Plexin-B1 deletion in AD: smaller footprints of plaque-associated glial nets, shift towards more compact amyloid plaques, and attenuated neurotoxicity.